Coseismic extension recorded within the damage zone of the Vado di Ferruccio Thrust Fault, Central Apennines, Italy

Harold Leah[a,1,*], Michele Fondriest[a], Alessio Lucca[b], Fabrizio Storti[b], Fabrizio Balsamo[b], Giulio Di Toro[a,c,d]

[a] School of Earth and Environmental Sciences, The University of Manchester, M13 9PL, UK

[b] NEXT – Natural and Experimental Tectonics Research Group, Università degli Studi di Parma, Dipartimento di Scienze Chimiche, della Vita e della Sostenibilità Ambientale, 43124 Parma, Italy

[c] Istituto Nazionale di Geofisica e Vulcanologia (INGV), Via di Vigna Murata 605, 00143 Roma, Italy

[d]Dipartimento di Geoscienze, Università degli Studi di Padova, Via G. Gradenigo 6, 35131, Padua (Italy)

[1] School of Earth and Ocean Sciences, Cardiff University, Main Building, Cardiff, CF10 3AT, UK

*Corresponding Author Details

Email: LeahHR@Cardiff.ac.uk

Graphical abstract

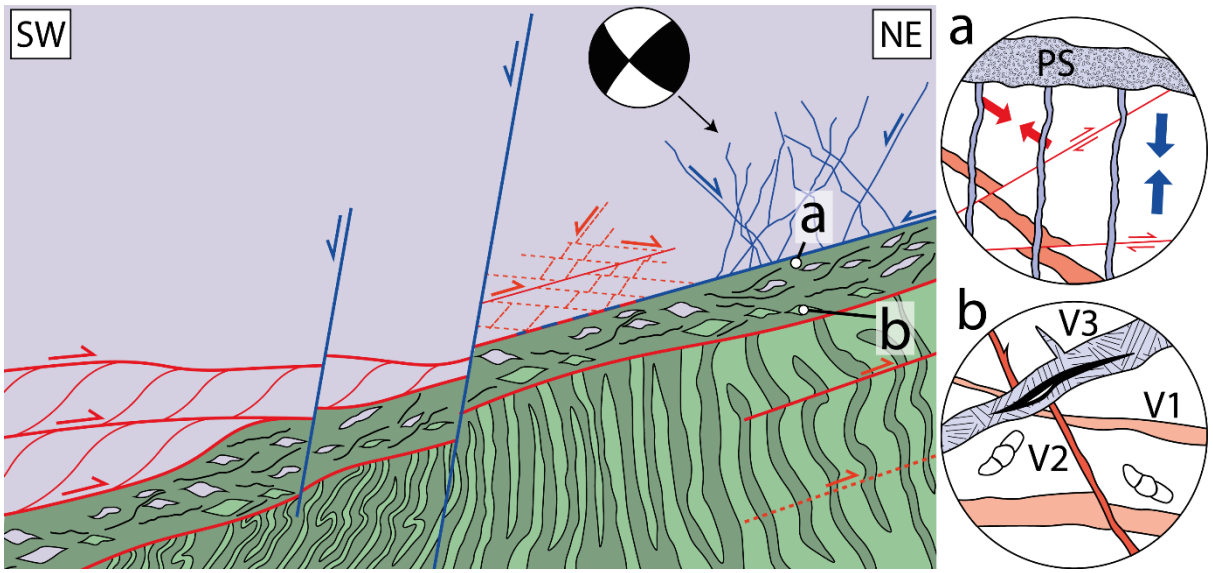

Highlights

1. Fault core observations indicate stable pressure solution-mediated aseismic thrusting
2. Mirror-like normal faults indicate extensional fossil earthquakes in the hangingwall
3. Hangingwall extension kinematics are similar to those of low angle seismic sequences

Abstract

Recent high resolution hypocentral localisation along active fault systems in the Central Apennines illuminates the activation of seismogenic volumes dipping at low angle (< 30°) in extensional settings overprinting contractional deformations affecting the continental crust of the Adria microplate. Individuation of the geological structures and of the fault processes associated with these seismic patterns will contribute to the interpretation of seismic sequence evolution, and seismic hazard studies.

Here we report field and microstructural evidence of seismogenic extensional faults localized within pre-existing thrust fault zones. The Vado di Ferruccio Thrust Fault (VFTF) is a narrow fault zone (<2.5 m thick fault core) in the Central Apennines of Italy, accommodating ~1 km of shortening during Miocene-Pliocene and exhumed from < 3.5 km depth. In the thrust zone, exposures throughout the Fornaca Tectonic Window show Late Triassic bituminous dolostones thrust over Middle Jurassic interlayered carbonates upon a SSW-dipping fault. Isoclinal folds are dragged and sheared by thrust-parallel reverse faults in the footwall block whereas NW-striking faults occur within the hanging wall. Fault core observations are consistent with stable pressure solution-mediated aseismic sliding towards N024° during thrusting, with cyclic veining and faulting. Later extension has been accommodated at the regional scale by major normal faults cutting through the VFTF, while veins and pressure-solution seams crosscut the microstructures associated with thrusting and record the extensional stress regime within the thrust fault core. Lenses of shattered rocks (up to 10s m thick), cut by a dense network of small displacement (<1.2 m) mirror-like normal faults, are reported in the hangingwall of the VFTF. These minor faults, related to a sharp principal slipping surface on the upper margin of the VFTF fault core, are interpreted as fossil evidence of microseismicity compartmentalized within the hanging wall of the VFTF. Synthetic and antithetic normal faults within the VFTF hangingwall damage zone are

geometrically and kinematically similar to small earthquake ruptures (M_w <2) in the hangingwall of low angle structures such as the thrust flats illuminated during the 2009 M_w 6.1 L'Aquila seismic sequence.

1 Introduction

Activation of extensional faults in the Central Apennines is associated with significant seismicity (Galli, 2002), including the 2009 M_w 6.1 L'Aquila (Chiaraluce et al., 2011; Valoroso et al., 2013) and 2016 M_w 6.5 Amatrice-Norcia (Michele et al., 2016; Chiaraluce et al., 2017) seismic sequences, both of which led to significant loss of life, infrastructure collapse and significant economic losses (Dolce and Di Bucci, 2017). These earthquakes typically occur on normal faults which cut through thick (4-8 km) sequences of carbonate rocks in the upper crust (Vezzani et al., 2010; Dolce and Di Bucci, 2017). Comprehensive and high-resolution monitoring and hypocentral relocation of seismicity in the region has provided important insights into the geometry of activated fault systems (Chiaraluce et al., 2011, 2017; Valoroso et al., 2013). For example, the 2009 L'Aquila seismic sequence was characterised by foreshocks which ruptured "high-angle" (i.e., dipping 50-60°) normal faults, and aftershocks which ruptured both high-angle and "low-angle" (i.e., dipping 15-25°) rock volumes (Chiaraluce et al., 2011; Valoroso et al., 2013), suggested to represent re-activated thrust faults (Falcucci et al., 2015). Normal faulting associated with low-angle structures has been studied in the field in the Alps (e.g. Cardello and Mancktelow, 2015), Northern Apennines (e.g. Clemenzi et al., 2015), and Gran Sasso Massif (e.g. Demurtas et al., 2016) where normal faults were shown to be exhumed analogues of seismically-active normal faults at depth. Investigation of the Vado di Corno Fault Zone showed in-situ shattering, formation of mirror-like slip surfaces, and highly-localised sheared calcite veins within a cataclastic unit resulting from multiple seismic ruptures on a high-angle normal fault (Demurtas et al., 2016). Intersecting the normal fault, an extensionally-reactivated low-angle thrust was inherited from earlier Pliocene compression and partially reactivated during later extension (Demurtas et al., 2016). This geometry is coherent with associated high-angle normal faults and low-angle volumes at depth seismically-activated during the 2009 M_w 6.1 L'Aquila earthquake

98 (Chiaraluce et al., 2011; Valoroso et al., 2013). To better understand the processes occurring
99 in seismically-activated low-angle fault zones in the Central Apennines we investigate the
100 Vado di Ferruccio Thrust Fault (VFTF), a thrust fault exposed further east in the Gran Sasso
101 Massif, and document localised coseismic extension compartmentalised within the
102 hangingwall block of the thrust.

103 Coseismic extension is used here to describe extensional slip occurring on a fault or a
104 fault network during a seismic event (earthquake). Coseismic extension on a thrust fault can
105 imply the reactivation of the low angle surface (i.e., negative inversion) formed during initial
106 compression or, as is documented here, localised extensional secondary faulting within the
107 damage zone of the thrust. This paper documents a case of coseismic extension within the
108 hangingwall damage zone of the VFTF in the Central Apennines, and shows how it is distinct
109 from compressional features formed during thrusting.

110 The VFTF was first described alongside the entire thrust stack exposed in the Gran
111 Sasso chain in the seminal paper of Ghisetti (1987) and mapped by Ghisetti and Vezzani
112 (1986), with the name "thrust 7" ($\varphi 7$ or T_7). The current study consists of an integrated field-
113 microstructural reappraisal of the VFTF architecture based upon this previous work. The
114 studied fault likely corresponds, at the regional scale, to the "Upper thrust" described by Pace
115 and Calamita (2015) on the north side of the Corno Grande and the Gran Sasso Massif
116 (Adamoli et al., 2012). Here, we prefer to use the name Vado di Ferruccio Thrust Fault
117 (VFTF) which strictly relates the studied thrust to its outcropping area. New techniques are
118 used here to discern the structure of the Vado di Ferruccio thrust zone from meso- to micro-
119 scale; detailed field investigation at selected localities is accompanied by microstructural
120 description of fault core samples using optical microscopy, field-emission scanning electron
121 microscopy, and micro-Raman spectroscopy. The resulting data is used to describe observed
122 microstructures, minerals, and previously undescribed amorphous materials. These

observations are then used to (i) determine mesoscale processes accommodating strain throughout the fault zone during compression and extension, (ii) establish kinematics of thrusting and normal faulting, (iii) infer deformation processes for compression and extension from microstructures and relate this to fault core lithology, and (iv) discuss whether there is evidence of seismic activation of the VFTF hanging wall, and if so, compare with microseismicity distributions of seismic sequences in the Central Apennines.

2 Geological Setting

2.1 Gran Sasso Massif

The Gran Sasso Massif is a fault-bounded area in the Central Apennines (Fig. 1b) containing the highest peaks of the mountain range. It was formed by Miocene-Pliocene thrusting of Triassic to Pliocene age rocks during the westward subduction of the Adriatic slab beneath the European Plate (e.g. Devoti et al., 2008; Cardello and Doglioni, 2015). The massif axis trends N-S in the eastern part and WNW-ESE in the central and western parts, reflecting inherited Jurassic palaeogeography and faulting (Speranza, 2003; Adamoli et al., 2012; Cardello and Doglioni, 2015). The range is bounded on its south side by a 30 km long segmented normal fault system (the Campo Imperatore fault system; Galadini and Messina, 2004). The north side of the massif consists of approximately 2000 m high cliffs, exposing multiple stacked folds and thrusts in thick carbonate successions (Ghisetti, 1987; Ghisetti and Vezzani, 1991; Vezzani et al., 2010). Thrusting in the Gran Sasso area propagated from west to east from the Miocene-Pliocene, with increased deformation intensity on deeper thrusts (Ghisetti, 1987). Transport was towards the north-east (Ghisetti and Vezzani, 1991), accommodated by slip along the E-W trending thrusts on the north side of the range and increasing towards the east (Ghisetti and Vezzani, 1991; Adamoli et al., 2012). Thrusting

may have rotated pre-existing Mesozoic normal faults to younger-on-older low-angle summit faults (Pace et al., 2014; Pace and Calamita, 2015)

Thrusting at ~7 Ma was followed by back-arc extension, which propagated eastward from the Early to Middle Pleistocene onward (Ghisetti and Vezzani, 2002). The frontal margin of active extension is demarcated by the Gran Sasso range (D'Agostino et al., 1998; Ghisetti and Vezzani, 1999; Galadini and Messina, 2004).

Figure 1 here

2.2 Fornaca Tectonic Window

The study area is localized in the Gran Sasso Range and encompasses the "Fornaca Tectonic Window" (FTW), situated in the Fornaca Valley on the northern border of Campo Imperatore plain (Fig. 1a). Campo Imperatore is an intra-mountain basin (1700-1900 m) bordered by Quaternary active seismogenic faults (Galli, 2002; Demurtas et al., 2016). WNW-ESE trending ridges, bounded by these normal faults, contain the peaks of the eastern Gran Sasso Massif; including Mt. Prena, Mt. Camicia, and Mt. Brancastello on the north side (Fig.1a).

The Fornaca Valley is a lightly-vegetated valley between Monte Prena and Monte Camicia with two thrust faults exposed within it. On the upper east side of the valley, an upper out-of-sequence thrust fault (Fig. 1c) is noted for its emplacement of younger rocks upon older (Ghisetti, 1987; D'Agostino et al., 1998). At the base of the valley, the Vado di Ferruccio Thrust Fault (VFTF) has been exposed by erosion to form the FTW (Fig. 1a & c). The VFTF places Upper Triassic bituminous dolostone (*Dolomie Bituminose*) upon Middle Jurassic carbonate grainstones (*Corniola*) and marls (*Verde Ammonitico*) (Fig. 1c & d). Several normal faults cut the VFTF in the tectonic window (Fig. 2), offsetting it by 10-30m in places (Ghisetti and Vezzani, 1986).

Most work in the Fornaca Valley has been focused on the kinematics of the out-of-sequence thrust (T_1 *sensu* Ghisetti 1987, Fig. 1c) near the summit of Monte Camicia (Ghisetti and Vezzani, 1991; D'Agostino et al., 1998; Adamoli et al., 2012; Pace et al., 2014; Pace and Calamita, 2015). The footwall of this thrust is composed of crystalline and bituminous dolostone (Fig. 1d) sitting in large-scale recumbent chevron folds trending E-W and verging north (Ghisetti and Vezzani, 1986, 1991; Ghisetti, 1987). These folded dolostones represent the hanging wall of the VFTF (T_7 in Ghisetti 1987, Fig. 1c) within a large duplex structure; similar folding has also affected the footwall Jurassic carbonates (Fig. 1c), attributed to the exploitation of bedding and mechanically weaker layers during thrusting (Ghisetti and Vezzani, 1986, 1991). The overriding thrust fault (T_1 in Ghisetti 1987) is steeper than the VFTF and truncates it near the base of the valley (Fig. 1c). Thrust plane-bedding cut-offs indicate a transport direction of N020, temporally constrained by synorogenic sedimentation in the Laga and Cellino basins and the Adriatic foredeep as Messinian-early Pliocene (Ghisetti and Vezzani, 1991).

Detailed field description of the fabrics and structures of the thrust stack, the VFTF in particular, was undertaken by Ghisetti (1987). The VFTF principal slip surface was characterised as having large-scale undulations (10s to 100s meters) associated with thrust duplexes, upon an overall convex-up geometry. Within duplexes, dolomitic lenses from the hanging wall show abundant cataclastic textures, whereas pure to marly limestone lenses from the footwall show evidence of both cataclasis and pressure solution. Deformation structures observed within these duplexes are stated to be the result of localized shear between contrasting lithologies. Foliated fault rocks, mainly developed within marly limestones, contain S-C fabrics (e.g. Koopman, 1983) and Riedel shear surfaces (e.g. Tchalenko, 1970; Davis et al., 2000; Katz et al., 2004) associated with cataclasite microlithons. The S surfaces rotate and converge into thrust-parallel microshears, intersecting

with C microshear surfaces at angles of 30-40°. Microshears are thought to accommodate slip of microlithons, which acted as a rigid obstruction during deformation in the core of the VFTF. Deformation was concentrated in the marly portions of the core of the VFTF, where pressure solution and grain crushing were dominant (e.g. Fig. 11 of Ghisetti, 1987). At the thin section scale, the occurrence of fine grained brown material is attributed to organic carbon within the *Dolomie Bituminose*. Pull-apart regions show syn-tectonic fibrous calcite growth and veins, which contain sparry calcite, are deformed where they intersect micro-shears at a high angle. Such features suggest early vein formation prior to deformation along with the host rock. This study builds on this previous work by Ghisetti (1987); deformation mechanisms in the thrust are discerned and greater consideration is given to the later extensional deformation phase in the area.

2.3 Lithologies adjacent to the VFTF

Deposition of the units lying in the hanging wall of the VFTF began in the Late Triassic with widespread transgression due to rifting associated with the opening of the Neotethys ocean (Adamoli et al., 1990; Ciarapica, 2007). Approximately 180 m of organic-rich, planar-laminated dolostones (*Dolomie Bituminose*) containing anhydrite and chert nodules are exposed in the Fornaca Valley (Adamoli et al., 1990) (Fig. 1d). Up to 1.5 km total thickness of dolostones formed within localised, shallow basins during the early stages of the Late Triassic marine transgression (Centamore et al., 2002; Cardello and Doglioni, 2015). The basins were poorly interconnected and consequently euxinic (Adamoli et al., 1990; Barattolo and Bigozzi, 1996; Cardello and Doglioni, 2015). This preserved organic matter and limited faunal bioturbation, forming an organic carbon-rich planar carbonate in the lower thickness (Adamoli et al., 1990; Ciarapica, 2007).

The *Dolomie Bituminose* grades up into a more massive Early Jurassic dolostone (*Dolomia Principale*) (Fig. 1d), associated with shallow-water marginal facies before

lagoonal facies form poorly bedded grainstone lenses in the upper third of the sequence (Adamoli et al., 1990; Barattolo and Bigozzi, 1996). The *Dolomia Principale* formation is at least 600 m thick (Fig. 1c) at Monte Prena (Barattolo and Bigozzi, 1996) and contains very low organic content (Ciarapica, 2007). The gradual transition between the *Dolomie Bituminose* and the *Dolomia Principale* is visible in the hanging wall as one moves north along the thrust fault in the FTW.

Formations in the footwall of the thrust are described as pelagic with varying degrees of input from a strongly detrital supply. Micritic cherty limestones are interbedded with marly layers 0.5-1 m thick in the Middle Jurassic-age *Corniola,* where brachiopods and ammonites are reported (Ghisetti and Vezzani, 1986; Bertinelli et al., 2004). Lithologies gradually become more marl-rich in the overlying Middle-Late Jurassic *Verde Ammonitico* (Ghisetti, 1987) (Fig. 1d). The Cretaceous to Oligocene age carbonates in the succession correspond to the base of the slope connected to the adjacent Lazio-Abruzzi carbonate platform (Van Konijnenburg et al., 1999).

3 Methods

Orthorectified photographs from the 2009 20 cm resolution aerial survey (available at www.regione.abruzzo.it/xcartografia) were used, in conjunction with elevation data, field photographs, field sketches, and previously published geological maps (Ghisetti and Vezzani, 1986), to trace major tectonic surface outcrops in the area using ArcGIS 10.3 software. Elevation data was used from the 10 m cell grid size TINITALY/01 digital elevation model (Tarquini et al., 2007, 2012).

Ten localities within the FTW were selected for the systematic measurement of orientations and lineations (where present) of faults, veins, fractures, and folds. Orientation measurements of features associated with exposures of normal faults in the hanging wall of

247 the VFTF (fault plane and lineation, exposure orientation, marker orientation) were used to
248 calculate absolute displacement in the lineation orientation. Localities were mostly situated in
249 the southern half of the tectonic window since previous work showed abundant structural
250 data collection in the northern part of the area (Ghisetti and Vezzani, 1986) and because
251 outcrop exposure was better due to stream incisions. Measurements were plotted onto
252 stereonets using Stereonet 9 (Allmendinger et al., 2011; Cardozo and Allmendinger, 2013).
253 Thirty oriented samples of fault rocks were collected of structurally significant
254 features within the core of the VFTF. To investigate the effect of fault geometry, sampling of
255 the fault core was performed at localities where the VFTF showed different dip angle. Ten
256 polished thin sections, cut parallel to the slip direction and orthogonal to the foliation of each
257 sample, were produced at the School of Earth and Environmental Science, The University of
258 Manchester. Some delicate samples were set in thermosetting resin to maintain the internal
259 structure during sample preparation. Thin sections were scanned at high resolution to provide
260 a reference image prior to any microanalytical work.
261 Optical microscopy, using both transmitted and reflected light, was used to determine
262 the cross-cutting relationships visible at the thin section scale, and to identify areas suitable
263 for further analysis using scanning electron microscopy and micro-Raman spectroscopy.
264 Transmitted light photomicrographs were, when necessary, stitched together using Microsoft
265 ICE (http://research.microsoft.com/enus/um/redmond/groups/ivm/ICE/). Micro-Raman
266 spectroscopy was performed with a 532-nm green laser on untreated thin sections using a
267 Horiba XploRA Microscope Raman System at the Nanoscale Imaging and Analysis Facility
268 for Environmental Materials (NIAFEM) at the University of Manchester. Spectra obtained
269 from this operation were adaptively baseline-corrected using Spectragryph software
270 (www.effemm2.de/spectragryph/) and the resultant data was compared to spectra of known
271 minerals from multiple databases (including the Bio-Rad Raman Spectral Database and the

Romanian Database of Raman Spectroscopy) to qualitatively determine mineralogy and nature of any amorphous material in the samples. Thin sections of two samples from each thrust fault core locality and three from the hanging wall adjacent to the fault core were selected for analysis using electron microscopy. Backscattered electron images and energy-dispersed spectra were collected with either a FEI Quanta 650 Electron Microscope or Philips/FEI XL30 Field Emission Gun Environmental Scanning Electron Microscope, both at NIAFEM, in the School of Earth and Environmental Science at The University of Manchester. Backscattered electron images and energy-dispersed spectra were acquired at 15 KeV and standard spot size.

Figure 2 here

4 Field observations of the Vado di Ferruccio Thrust Fault

Thrust zone features vary throughout the study area but are dominantly associated with faulting in the dolomitic hanging wall and folding with minor faulting in the mixed carbonate footwall. The main features are presented here prior to description and data relating to structural features in the hanging wall (HW), footwall (FW) and fault core throughout the FTW. Field descriptions and structural data from more than ten localities are presented to illustrate the variation in structure within the tectonic window (Figs. 2 & 3).

Figure 3 here

4.1 The Fornaca Tectonic window

The VFTF dip angle varies over tens of metres throughout the FTW from 11° to 50°, significantly steepening in the north-west of the area despite a generally convex-up geometry elsewhere in the tectonic window (Fig. 2). Strike also varies locally between 090 and 140 (strike and dip data are given from N azimuth), trending E-W in the north and NW-SE in the south (Fig. 3). Near vertical normal faults offsetting the core of the VFTF by 5-15 metres

297 strike NW-SE (Fig. 2). Normal fault surfaces are sharp with clay-smear defining sub-vertical
298 lineations (Fig. 3, locality 6).

299 **Figure 4 here**

300 *4.2 Hanging wall block*

301 Fault slip surfaces are abundant in the hangingwall with variable orientation, shear
302 sense, and surface texture (Figs. 3, 4a, 4b). Reverse faults, subsidiary to the principal thrust
303 slip surface, typically form at low angle and rarely form lineations on slip surfaces (Figs. 2 &
304 3, localities 2, 4, 5, 8a, 8b, 9, 10). Normal faults form at high angle, often with well-defined
305 lineations on surfaces cutting low-angle slip surfaces (Figs. 2 & 3). Folding in the
306 hangingwall is rarely exposed, though where it is, heavily-faulted beds of *Dolomie*
307 *Bituminose* form metre-scale open (interlimb angle ~100°) folds with gently west-plunging
308 axes and N-S striking profile planes (Fig. 3, locality 10).

309 **Figure 5 here**

310 Faults in the dolomitic hangingwall often form in systematic orientations with
311 similarly-oriented surfaces showing consistent shear sense (Fig. 3, localities 2, 6, 8b, 10).
312 Thrust-parallel surfaces are common throughout the area (Fig. 3, localities 2, 8a, 10), often
313 coexisting alongside synthetic P and R surfaces. These surfaces often form mesoscopic
314 fabrics whereby bitumen-poor dolostone is faulted into lenticular blocks by a shallow (<20°)
315 and steeper (45-80°) set of S-dipping shear surfaces, often acute towards the NE (Figs. 3,
316 locality 8-1 & 5). Steeply-dipping (60-80°) normal shear surfaces cut both synthetic reverse
317 and thrust parallel shear surfaces (Fig. 5). Lineations on these SW-dipping normal surfaces
318 plunge steeply (60-80°) to the south (Fig. 5), indicating dip-slip movement. Where the
319 hangingwall is more bituminous, slip has occurred along the bedding in both normal and
320 reverse senses (Fig. 3, localities 4, 8b).

Bitumen-poor dolostones in the hanging wall are pervasively shattered up to ten meters from the thrust fault (Fig. 4a & b). These heavily fractured dolostones are cut by a dense network of highly-reflective mirror fault surfaces with dominant dip-slip kinematics (Fig. 3, locality 1). Bed-parallel slip was not observed. Fault orientations are widely scattered, though more SE-dipping surfaces were measured (Fig. 3, locality 1). Lineations on mirror surface faults are defined by smeared bitumen streaks and aligned truncated clasts parallel to slip direction (Fig. 6c & d). Lineations are oriented within a high-angle SW-striking band (Fig. 3, locality 1). Fault displacements up to a maximum of 1.2 m were constrained, exploiting the occurrence of displaced markers (e.g. rock laminations) and fault cross-cutting relations. These normal faults have a lateral continuity of few meters, are compartmentalized within the hangingwall block of the VFTF, and terminate upon a sharp principal slipping surface (PSS) bordering the top of the thrust fault core (Fig. 6a & b).

4.3 Footwall block

Steeply-dipping isoclinal folding in the FW is continuous along strike across the tectonic window. Exposures of folds, grouped by lithology, are described here in terms of geometry and association with faulting.

Figure 6 here

Folding in marl-rich lithologies is defined by thin (<15cm) beds of grainstone within a more abundant marl (Fig. 7a). Folding is isoclinal, N-verging, and cut by a handful of small-offset (<15cm) minor faults. Due to the isoclinal nature of the folding, bedding dips predominantly south at approximately 50°. The fold axes plunge gently west, defining (together with poles to bedding) a N-S profile plane across E-striking folds (Fig. 7a).

Isoclinal folding of more thickly-bedded (~1m) grainstone-rich lithologies with less marl is cut by low-angle south-dipping reverse faults, sub-perpendicular to bedding (Fig. 7b). Isoclinal folding is defined by steeply north-dipping bedding and verges to the south. Where

minor faults have no visible offset, minor recumbent shear folding of the isoclinal folds has occurred adjacent to thrust-parallel reverse faults, producing sinuously-undulating isoclinal folds of interbedded grainstones and marls near localised reverse fault surfaces (Fig. 7b). Recumbent folds have axial planes subparallel to minor fault surfaces. In the upper part of the exposure, low-angle reverse faults have offsets up to 3 m and form well-developed (~20cm thick) fault cores.

Strongly refolded isoclinal folding is exposed just beneath the thrust surface (Fig. 7c). Limbs of the recumbent fold dip moderately (~45°) to the SW and gently (20-30°) to the NE, the hinge plunges to the NW. The core of the main thrust fault, which dips 25° to the S, truncates the fold limbs (Fig. 7c). Marl-rich beds within refolded folds have been incorporated into marl-rich fault core above. The profile surface of the fold trends on average NE-SW, though poles to bedding are spread as the fold hinge varies locally in orientation (Fig. 7c).

Figure 7 here

4.4 Fault core

The fault core of the VFTF is well developed throughout a variety of lithologies, maintaining a thickness of 0.5-2 m throughout the area (Fig. 8). Occasionally, a sharp ultracataclasite-bearing PSS on the upper surface of the fault core forms a measurable lineation, with clay smearing or alignment of grains (Fig. 6a & b). Structure within the fault core varies throughout the area but generally consists of foliated cataclasite with lenticular sheared lithons within a phyllosilicate-defined S-C fabric. Larger lithons often contain subvertical veins perpendicular to thrust plane orientation. Angles between S and C planes are around 30° (Fig. 3, locality 1). Some minor extensional surfaces cut the fabric at high angles, oblique to the thrust (Fig. 3, locality 1), these surfaces do not cut the PSS.

Fault core lithology and fabric varies significantly throughout the area (Fig. 8); bitumen is more common in the south of the area and fabrics become increasingly clast-dominated in the north of the area (Locality locations indicated in Figs. 2 and 3). Foliated cataclasites are categorised as marly lithologies (blue on Fig. 8), S-C fabrics within these encompass sheared clasts up to 20 cm long. Relative proportions of marl and clasts varies from marl-dominated to clast-dominated unsystematically between localities. Locally marl-enriched (up to 100%; Fig. 8) areas are associated with m-scale duplexes which occur at localised irregularities in thrust orientation, often associated with later normal faults (Fig. 5).

Fractured lithologies (green on Fig. 8) do not contain calcite veins characteristic of the veined lithologies also described below. Fractures occur commonly as part of the hangingwall damage zone above the PSS but are more common in the fault core where *Dolomie Bituminose* is present in moderate to significant amounts (<80%). Veined fault rocks (yellow on Fig. 8) appear brown in the field, with voids filled in with calcite. Veined fault rocks occur in abundance in the upper part of the fault core (<90%), often adjacent to the PSS and hanging wall dolomite. Bituminous fault rocks (purple on Fig. 8) are so called due to the dark material present within. This material is attributed to amorphous carbon within the *Dolomie Bituminose*. Dark material is often associated with marl or cataclasite in the upper part of the fault core in small to moderate amounts (<35%).

Figure 8 here

5 Microstructure and mineralogy of the Vado di Ferruccio Thrust Fault

Microstructural observations from the thrust fault core are presented for clay-rich and clay-poor samples. Within each group of samples, features are often similar. The structure and mineralogy of each type of fault core “lithology” are described. A summary table of observations and interpretations is provided at the end of the section (Table 1).

5.1 Microstructure and mineralogy of clay-rich fault core rocks

Clay-rich fault rocks are characterized by an heterogeneous assemblage with domains strongly affected by pressure solution and local clay enrichment embedding other more cataclastic domains (Fig. 9a-d). R-type shears consistent with thrusting are widespread within these fault rocks and normally dissect both domains (Fig. 9b, c & d).

Figure 9 here

Cataclasite-dominated regions are composed of either homogeneous calcite or dolomite (Fig. 9f & g), with occasional quartz grains. Sparse, immature, sub-horizontal pressure solution seams cut a very fine ultracataclastic (grain size <100 μm) dolomitic matrix with gently (15°) south-dipping surfaces (Fig. 9d). Grains within fine cataclastic lenses are angular and affected by intense fracturing. Sub-vertical calcite veins up to 150 μm wide cut through the cataclastic lenses (Fig. 9d, g, h & i) perpendicular to pressure solution seams, which often truncate them (Fig. 9h & i).

Pressure solution-rich regions are up to 5 mm thick and mainly consist of foliated clays with sheared clasts of cataclastic material up to 1 mm in size. Pressure solution seams contain a mixture of iron oxides, amorphous carbon (Fig. 9e), and clays. Clays occur in localised seams along mineralogical contrasts adjacent to grains and veins. Two sets of veins can be discerned within pressure solution-rich regions dipping NE and SW, respectively. NE-dipping veins are up to 80 μm wide and are truncated by thrust parallel shear surfaces, SW-dipping veins are up to 30 μm wide and are continuous through these microshear surfaces (Fig. 9h).

R-type shear surfaces dip north at 40-60°, offsetting cataclastic and pressure solution-dominated domains by up to 1 mm (Fig. 9b & c). These shear surfaces are most dominant at the top of the fault core, within five centimetres of the PSS on the fault core's upper boundary (Fig. 9a). Further down into the core they are generally less developed. Significant amounts

of clay and oxide rich material have developed upon the R-type shear surfaces, truncating south-dipping veins (Fig. 9h & i). R-type shear surfaces converge with well-developed sub-horizontal pressure solution seams which cut across the whole fabric (Fig. 9b-d).

5.2 Microstructure and mineralogy of clay-poor fault core rocks

Clay-poor lithologies, sampled from sheared lithons within the thrust core, exhibit a diverse range of matrix types and deformation features. These features include veins, pull-apart structures, cataclastic fabrics, microfaults, and minor localised pressure solution (Table 1).

Figure 10 here

The mineralogy of clay-poor lithons is mostly homogenous calcite (Fig. 10a), though some dolomitic lithons are present. Matrix textures vary throughout clay-poor lithons; intact textures include crystalline twinned calcite encompassing recrystallised fossils (Fig. 10b) and peloidal grainstones, while some samples display significant cataclasis and microfaulting. At least three vein sets are present within the lithons: a fine-grained low angle NE-dipping set up to 100 μm wide; a sub-vertical set up to 50 μm wide with a sub-horizontal opening direction and fine-grained crystals near the margins; and a coarse-grained vein set enveloping locally clay-rich pressure solution material within both sub-vertical and sub-horizontal veins (Fig. 10a). Within intact calcitic matrices, pull-apart structures up to 300 μm long and 100 μm wide are present.

Cataclastic textures are also present within clay-poor lithons. Sub-horizontal and ~30° north-dipping bands of finer (<10 μm) material lie between heavily fractured grains of calcite and minor quartz up to 1 mm in size. Rarely, partially-intact cataclastic grains show wavy and complex twinning. Larger twins up to 15 μm wide contain smaller high angle twins (<2 μm in size) and cross-cut thinner (<3 μm in size), more numerous sub-horizontal twins. Some recrystallization of twins and the matrix is visible as fine grains. Calcite veins within

cataclastic fabrics do not show twinning and tend to form normal to the PSS. Pressure solution seams up to 100 μm thick follow irregular paths through homogeneous clay-poor lithons, often coinciding with dolomitic bands or quartz grains and truncating some veins (Fig. 10a, c & d). Some veining has exploited these pressure solution seams; these veins correlate with dark sub-vertical veins visible in clay-poor lithons in the field (Fig. 10c & d).

Table 1 here

6 Discussion

6.1 Thrusting on the VFTF

6.1.1 Deformation mechanisms within the thrust fault core

Dominant deformation mechanisms accommodating strain within the fault core are cataclasis, diffusive mass transfer in the form of pressure solution, and veining. The prevalent deformation mechanism varies throughout the thrust core between more localized fracturing and veining in clay-poor crystalline carbonate lithons and more diffuse deformation within clay-dominated foliated cataclasites (cf. Ghisetti, 1987). This complexity arises from the mixing of hangingwall and footwall lithologies, highlighted by small-scale duplexes and sharp boundaries between distinctly-deforming domains and noted by Ghisetti (1987; Fig. 5). Fault rock microstructures are grouped and discussed based upon clay content, their microstructural attributes, and inferred active deformation mechanisms (see also Table 1).

The S-C fabrics within the fault core are defined by foliated cataclasites around sheared lithons. The S and C surfaces are acute towards the NNE, perpendicular to a vertical plane striking 024, implying thrust transport towards the NNE. This is similar to that discerned by Ghisetti (1987) from similar S-C fabrics on the VFTF. Within clay-poor fault core lithons, the dominant deformation mechanisms are cataclasis and veining. Lithons with homogenous fine-grained calcite preserve three vein generations cross-cutting the matrix (Fig. 10a). Multiple generations of veins with distinct orientations suggest multiple veining

events under variable stress conditions occurred on the VFTF. Vertical veins (V2 on Fig. 10) cut NE-dipping veins (V1 on Fig. 10) and could be associated with either extensional (Sibson, 2000) or compressional deformation. Compression would cause vertical vein formation by increasing overburden as thrust sheets are emplaced on overlying thrust faults within the Gran Sasso thrust stack. Both sets of veins (NE-dipping and vertical) are cut by larger, more continuous veins with no distinct orientation (V3 on Fig. 10). Here, both NE-dipping and vertical veins (V1 and V2) are attributed to compression and larger, more continuous veins (V3) are attributed to extension due to their dissimilar structure and cross-cutting nature indicating more recent formation. Regardless of associated stress conditions, vein textures in clay-poor lithons suggest fluid circulation during discrete deformation phases formed distinct sets of veins.

In foliated fault core samples incorporating clays in moderate to rich amounts, strain accommodation is partitioned between cataclasis, frictional sliding upon clays or carbon-coated surfaces, and pressure solution. Enrichment of insoluble species within pressure solution seams (Fig. 9i, 10c) suggest diffusion-mediated pressure solution was prevalent (Bos and Spiers, 2001; Gratier et al., 2013b), aided by initial grain-size reduction by cataclasis. Incorporated and authigenic clays may have aided aseismic stable sliding, which accommodated the majority of slip. The R surfaces offsetting regions of pressure solution (Fig. 9b, c & d) are consistent with northward thrusting, suggesting cyclic pressure solution and cataclasis with veining during compression. Veining events are better preserved within the monomineralic matrix of clay-poor lithons (Fig. 10a) than in the clay-rich areas where heterogeneous mineralogy aided pressure-solution mediated slip within the fault core. Furthermore, recrystallized fossils alongside preserved vein sets (Fig. 10b) within lithons show that some lithons stayed intact during thrusting and cataclasis was not pervasive throughout the core.

Cataclasis during early deformation on the VFTF, overprinted throughout the fault core (Figs. 9 & 10), decreased porosity and would have trapped upwelling fluids (Storti et al., 2003; Billi, 2010). Incorporation of clays from the footwall marl into the fluid-rich fault core during subsequent frictional sliding would have accelerated the onset of pressure solution (Hadizadeh, 1994; Gratier et al., 2013a). Abundant pressure solution within the core (Fig. 9) led to the production of authigenic clays by diffusive mass transfer (Rutter, 1983; Viti et al., 2014) and aided frictional sliding on clays and carbon. This is one way in which regions of high strain positively feedback to concentrate deformation within the same regions of the fault core. Diffusive mass transfer could also achieve further porosity reduction within the fault core by the growth of authigenic clays perpendicular to fluid transport direction and decreased pore volume by grain tip removal (Rutter, 1983; Yasuhara et al., 2005). Reduced porosity may lead to over-pressuring of fluids ($P_f > P_c$) forming north-dipping veins, though the localised and discontinuous nature of veining (Fig. 9h & i) suggests it is probably the result of extension perpendicular to the orientation of maximum compression defined by adjacent pressure solution seams (Hadizadeh, 1994).

Vein formation and sealing, possibly accompanied by healing at grain tips by mass transfer (e.g. Yasuhara et al., 2005), would strengthen the fault core. Shear of this re-strengthened fault core could cause a reversion to cataclastic deformation, forming the observed R surfaces which offset areas of pressure solution (Fig. 9b-d; Hadizadeh, 1994) and truncate north-dipping veins (Fig. 9i). Cataclasis of these regions of the fault core after veining could also result from localisation of strain away from sealed veins or by smearing and incorporation of weak phyllosilicate or carbon horizons during frictional sliding. Shear surfaces occur in orientations corresponding to steepened YPR shear planes (Tchalenko, 1970) and incorporate layers enriched in carbon liberated from carbonate by dissolution during pressure solution (Fig 9e). Shearing on R surfaces was therefore aided by pressure

solution (Gratier et al., 2013a) which continued to accommodate lesser amounts of slip. Microstructures upon shear surfaces appear consistent with weak-phase frictional sliding (Rutter et al., 2013; Tesei et al., 2013), perhaps of clays or carbon concentrated there during sliding.

Deformation of clay-enriched core lithologies represents a complex interaction of mechanisms, each altering fault core rheology based upon the properties of its products. This feedback is not seen within clay-poor fault core lithons, perhaps due to higher strain rates than be accommodated by pressure solution or more homogenous lithology limiting grain-boundary diffusion (Gratier et al., 2013b; Tesei et al., 2013). The abundance of weak clays and pressure solution seams within clay-enriched domains (Fig. 9d) implies that the thrust, at some stage probably early in its history, accommodated diffuse strain and gradual slip by stable sliding (Gratier et al., 2011, 2013b; Tesei et al., 2014). The heterogeneity of structures associated with the VFTF indicates this likely changed during slip on the thrust, with transient periods of diffuse shear transitioning to slip on more localised surfaces seen throughout the fault core (Fig. 8). Cyclic veining and cataclasis indicate the build-up of fluid overpressures and fracturing followed by fault core re-strengthening (Fig. 11g & h); Caine et al., 1996; Yasuhara et al., 2005; Woodcock et al., 2007; Cardello and Mancktelow, 2015; Clemenzi et al., 2015).

6.1.2 Deformation mechanisms and fault kinematics during compression in the fault damage zone

Hangingwall

Compressional hangingwall faults corresponding to Y, R, P and rotated Riedel surfaces indicate a NE-ward thrust transport direction (Fig. 3, locality 4), though lineations upon planes to corroborate this are sparse. Riedel surfaces intersect at a line oriented 9.3/117.6 (plunge/trend), perpendicular to the transport direction. Mesoscopic S-C structures

within HW dolomite are often acute to within ten degrees of the core-derived transport direction (034; Fig. 3, locality 8-1), but there is significant variability in this throughout the area (Fig. 3). Planes and lineations on faults forming the borders of dolomitic lenses within thrust duplexing indicate local variability in transport direction over tens of metres (Fig. 5). The rotation of strike of the principal thrust surface in the upper part of the Fornaca valley (Fig. 3, localities 6 & 7) is perhaps an indicator of more northward thrusting or local adjustment to accommodate more competent footwall lithologies (Ghisetti, 1987; Ghisetti and Vezzani, 1991).

Footwall

Complex refolded isoclinal folding in the footwall reflects lithological response to diffuse, then localised, shear. Initial compression led to the folding of footwall units to isoclinal geometry, with limbs dipping steeply to the S, implying significant shortening. As the VFTF developed, different lithologies within the footwall *Corniola* adjacent to the thrust responded in distinct styles (e.g. Lena et al., 2015). Marl-rich lithologies were subject to more diffuse shear strain, with dragging of the isoclinal fold limbs to the north and minor faulting. The axial planes of marl-rich folds have then progressively rotated towards the thrust fault orientation in relation to the gradual accommodation of shear strain within the fault core (Ramsay, 1980; Ghisetti, 1987).

Bouma sequences preserved within the *Corniola* beds comprise depositional clay-rich bands in their upper parts, which favoured bed-parallel slip (Bullock et al., 2014). Refolding of isoclinal folding is perpendicular to inferred transport direction and the fold axes varies locally, characteristic of shear folding (Ramsay, 1980; Ghisetti, 1987). Low-angle reverse shear surfaces emanate from the thrust and are less well-developed away from the thrust, indicating the main thrust core was the site of the majority of shear strain. Minor reverse faults may represent periods of main thrust core strengthening causing propagation of minor

570 thrusting into footwall lithologies in a small-scale ‘piggyback’ thrusting episodes (Ori and
571 Friend, 1984) to accommodate compressional strain by de-localisation away from the thrust
572 core (Wojtal and Mitra, 1986; Lena et al., 2015). Is it possible each of these surfaces locked
573 before forming the surface beneath, or, conversely, these surfaces developed
574 contemporaneously, accommodating lesser strain upon each. The orientation of the well-
575 developed shear folds sits perpendicular to N021, coherent with other results from kinematic
576 analysis of compression in both the work presented here and of Ghisetti (1987).

577 *6.1.3 Ambient conditions and displacement of the VFTF*

578 Analysis of kinematic indicators throughout the hangingwall, footwall, and fault core
579 indicate thrusting on the Vado di Ferruccio was towards N024, with local variability over
580 tens of metres between N000 and N034. Distance of transport from stratigraphic offset is
581 difficult to accurately calculate due to: (1) the locally variable nature of units involved in
582 thrusting (Cardello and Doglioni, 2015), (2) variable thrust orientation and possible
583 reactivation in extension (Ghisetti and Vezzani, 1986; Ghisetti, 1987; Pace et al., 2014; this
584 paper), (3) the scarcity of literature describing the *Dolomie Bituminose* and its stratigraphic
585 relationships within the carbonate sequence present in the Central Apennines (Adamoli et al.,
586 1990; Barattolo and Bigozzi, 1996; Bertinelli et al., 2004), (4) folding complicating estimates
587 of stratigraphic offset. Nevertheless, assuming an average thrust dip angle of 25°
588 perpendicular to transport direction and a stratigraphic gap of 550m (between the top of
589 *Dolomie Bituminose* and the base of the *Verde Ammonitico*), the resulting transport distance
590 on the thrust plane is ca. 1.3 km ($h=o/\sin\theta$; h=distance of transport along thrust surface,
591 o=stratigraphic gap due to thrusting, θ=dip of thrust fault). This is likely a conservative
592 estimate due to the intensity of folding, pressure solution in the fault core, and subsidiary
593 fault structures, all of which could have increased the accommodated displacement.

Within the FTW, areas with steeper thrust orientations are associated with more competent grainstone lithology in the footwall while shallower thrust orientations correspond to regions overlying interbedded marls-grainstones in the footwall. Local variation in thrust fault geometry therefore records the effect of variable lithology adjacent to the VFTF on strain localisation during thrust fault propagation. The evolution of the principal thrust fault, from shallow SW-ward dipping in the south of the study area to steeper southward dip in the north of the area, defines a variable geometry for the VFTF of concave-up in the north-west of the study area and convex-up elsewhere. This has previously been attributed to a lenticular geometry of the Santa Colomba Thrust Sheet (Ghisetti, 1987), though the more competent lithology within the core of large-scale footwall folding is raised here as a potential source of ramping.

Ambient conditions (confining pressure and temperature) during thrusting can be constrained by combining various sources of data. Apatite fission track and vitrinite reflectance data from the *Dolomie Bituminose* samples in the Gran Sasso yielded maximum burial temperatures of 100-105°C between 35 and 15 Ma, maintaining up to 108°C at 10 Ma (Rusciadelli et al., 2005). Assuming no anomalous geotherm due to thermal subduction-related degassing, a standard geothermal gradient of 30°C km^{-1} yields a depth estimate of 3.33-3.60 km. Indeed, estimated the maximum stratigraphic thickness of formations overlying the *Dolomia Principale* in the Gran Sasso is 3.48 km (Cardello and Doglioni, 2015). This is highly variable between relative paleogeographic highs and lows (where it is significantly thinned) in the basin of deposition of these units (Cardello and Doglioni, 2015). Nevertheless, this may represent the maximum depth of thrusting, and perhaps peak ambient conditions during Miocene compression.

6.2 Extensional activity recorded in the VFTF core and hangingwall damage zone

618 Dominant normal faults in the study area clearly indicate that extension was the most
619 recent deformation mode active, overprinting compressional structures (Figs. 2 & 11f).
620 Microstructures within the fault core indicate a change, after compression, to an inverted
621 stress orientation containing a sub-vertical principal stress (Figs. 9h, i, 11g). High angle
622 compressional R shears within upper fault core samples have well-developed pressure
623 solution upon them, cutting the most recent veins. These surfaces would be low-angle due to
624 the dip of the fault core, optimally oriented for activation as pressure solution seams
625 perpendicular to a vertical σ_1, consistent with extensional stresses (Fig. 11g; Ghisetti and
626 Vezzani, 1999; D'Agostino et al., 2014). The least deformed veins within pressure solution-
627 rich regions are orthogonal to the dominant pressure solution seam orientation (Figs. 9h, i,
628 11g).. These veins would also be subparallel to a vertical σ_1 and corroborate the existence of
629 extensional stresses, likely associated with the collapse of the thrust stack. Aside from
630 millimetre-scale veins, meso-scale structures within the VFTF core show no evidence of
631 measurable extensional reactivation (Fig. 8), indeed major normal faults accommodating
632 regional extension cut through the VFTF core (Fig. 11f). Rather, a sharp surface upon the
633 upper margin of the thrust fault core delineates a boundary of extensional faulting between
634 the core and hanging wall damage zone (Figs. 6 & 8).
635 Lenses up to 10 m (measuring perpendicular to the average thrust plane) thick of
636 shattered dolostones are locally observed in the hangingwall damage zone just above the
637 thrust fault core. These heavily fractured dolostones (Fig. 4b) are cut by a dense network of
638 mirror-like fault surfaces (Fig. 6c) characterized by a wide distribution of plane orientations
639 and lineations (Figs. 3, locality 1 & 11a). Movement lineations on fault planes are distributed
640 around a NE-SW striking plane, with a clustering around steeply SSW-plunging dip-slip (Fig.
641 11b-d). The scattering in orientation of normally-faulted mirror surfaces and their lineations
642 is consistent with an extensional, possibly dynamic, collapse of the hangingwall block

643 associated with small seismic ruptures. Determined offsets of sampled extensional faults in
644 the hanging wall are up to 1.2 metres, though many show offset of a few centimetres or less.
645 The length of these faults is difficult to assess precisely, due to the limited outcrop exposure,
646 but is in the range of tens to a few hundred meters. These are therefore structures which could
647 have hosted small earthquake ruptures (M_w <2) (Wells and Coppersmith, 1994). The range of
648 fault lineations indicates a NE-SW normal dip-slip trend within the faulting scheme,
649 consistent with kinematic inversion of measured faults (Fig. 11e) and more general
650 extensional trends in the Gran Sasso (D'Agostino et al., 2009; Cardello and Doglioni, 2015).
651 The intensive shattering of the hangingwall is a localised phenomenon, most-strongly visible
652 in the SW part of the FTW directly adjacent to the fault core (Fig. 3, localities 1 & 5).
653 Elsewhere, low-angle north-dipping fault surfaces are present in the hangingwall adjacent to
654 the thrust core (Figs. 2 & 3, localities 4, 5 & 8b) which are probably R-shears formed during
655 compression (Fig. 11f). These fault surfaces could have been reactivated in extension
656 alongside the intensive localised hangingwall faulting but are far more systematic in
657 orientation and continuously-recognisable in exposure.

658 Lineations upon the highly-localised thrust principal slip surface are consistent with
659 the lineation distribution of extensional hangingwall faults (Fig. 11d), suggesting they may be
660 related. The principal slip surface could therefore represent a potential decoupling boundary
661 between the hangingwall block, associated with shattering and compartmentalized
662 extensional faulting (each mirror-like fault is associated with extremely localized shear
663 strain), and the thrust core (Fig. 11f). The mechanical basis for this interpretation rests upon
664 the contrast in materials between the dolomitic hangingwall and the marl-rich fault core and
665 footwall preventing fault propagation downward across the detachment. Fault propagation
666 across mechanically-heterogeneous layers has been numerically modelled by Welch et al.
667 (2009) who show that faults which nucleate in the layer with a higher coefficient of sliding

668 friction (the dolomitic hangingwall) upon microshears will not propagate into an adjacent
669 weak ductile layer (such as the marl-rich VFTF core) if the ratio of horizontal to vertical
670 stresses in the weak layer is high (<0.4). We suggest the contrast in frictional and mechanical
671 properties (e.g. stiffness) across the principal slipping surface is sufficiently different, perhaps
672 in concert with a high vertical-horizontal stress ratio, to inhibit the propagation of localised
673 mirror-like fault surfaces into the fault core or hangingwall, instead forming a layer-bound
674 fault set (Welch et al., 2009).

675 **Figure 11 here**

676 Abundant mirror surfaces within dolostones, such as those seen in the hanging wall
677 adjacent to the thrust (Figs. 4b, 6, 11), possibly represent evidence of coseismic shear strain
678 localization at high slip rates (0.1-1 m/s) (Fondriest et al., 2013, 2015; Siman-Tov et al.,
679 2015; Kuo et al., 2016). The association of shattered dolostones and small-displacement
680 mirror-like faults with variable orientations have been previously interpreted at a potential
681 record of earthquake rupture propagation through carbonates at shallow depth (<3 km;
682 Fondriest et al., 2015, 2017). Mirror surfaces seem to be less frequent within more bitumen-
683 rich HW lithologies in the south of the tectonic window. Within bitumen-rich dolostones,
684 weak phase smearing of amorphous carbon on fault surfaces is observed (Fig. 6d); this might
685 represent a mechanism to stably reduce friction coefficient (Oohashi et al., 2011; Rutter et al.,
686 2013). Smearing of dark material on mirror surfaces within moderately bituminous
687 lithologies (Fig. 6d) could be further investigated to better determine controls on
688 graphitisation of amorphous carbonaceous material (Oohashi et al., 2011; Kuo et al., 2014),
689 associated controls on fault friction, and promotion of seismic slip by carbonaceous material.

690 **Figure 12 here**

691 Monitoring of seismicity during the 2009 L'Aquila earthquake sequence (main shock
692 M_w 6.1) highlighted the potential activation of inherited compressional structures at

693 hypocentral depths of < 3-4 km (Valoroso et al., 2013; Fig. 12), similar to the exhumation
694 depth of the VFTF. Indeed, minor earthquakes (mainly aftershocks with $M_w < 3$) were
695 illuminating low angle regional structures compatible with Miocene-Pliocene thrust flats.
696 Focal mechanisms of these events (Fig. 12) may be irregularly consistent with normal
697 activation of low-angle thrust flats, but mainly correspond to high-angle antithetic faults
698 (Chiaraluce et al., 2011; Valoroso et al., 2013). In the case of the VFTF, the negative
699 inversion of the pre-existing thrust flat (*sensu* Bigi, 2006) was not documented: the fault core
700 preserves evidence of stress inversion at the microscale (Fig. 11f) but it is cut by regional
701 normal faults. Conversely, shattering, and diffuse microfaulting (mostly high angle synthetic
702 and antithetic normal faults; Fig. 11e, f) registered the local extensional collapse of the
703 hanging wall damage zone, possibly during dynamic seismic activity.

704 **7 Conclusions**

705 Field and microstructural study of the structure and lithology throughout the Fornaca
706 Tectonic Window has shown the Vado di Ferruccio Thrust Fault accommodated at least 1.3
707 km of displacement towards N024. A combination of cataclastic and pressure solution-
708 dominated deformation took place within the marl-rich fault core where the compression was
709 most likely accommodated by stable aseismic creep. Intermittent fluid pressure build-ups
710 within the creeping fault core caused cyclic vein generations and cataclasis. The hanging wall
711 damage zone accommodated compression by sliding on minor, systematically-oriented faults.
712 Deformation in the interlayered carbonate footwall damage zone was dominated by isoclinal
713 folds, which were refolded by dragging in marl-rich areas or shearing on thrust-parallel
714 reverse faults in more competent grainstone-rich areas.

715 Subsequent extensional stress is recorded at the micro-scale on the VFTF, but no
716 measurable displacement is recorded. Microstructures within the clay-rich thrust fault core
717 register a late rotation of the applied stress field consistent with southward normal inversion.

Asymmetric strain across the fault core formed a sharp localized principal slip surface on the upper margin which acted as a decoupling surface between the fault core and the hangingwall damage zone and possibly accommodated a small extensional strain component. Extensional activity is instead well registered in the hangingwall damage zone where, locally, lenses up to 10 m thick of shattered dolostones are cut by a dense network of normal faults with mirror-like finish. These mirror faults display scattered orientations and are suggested to have formed by dynamic processes during rapid coseismic slip. In particular, the association of local bodies of intensely fractured wall rocks cut by small displacement highly localized fault surfaces has been interpreted as the result of microseismicity (M_w <2) occurring in the hangingwall block of a low angle extensional fault.

Small synthetic and anthitetic normal faults surfaces within the VFTF hangingwall damage zone are shown to be kinematically similar to structures rupturing during small (microseismic) earthquakes (M_w <2) in the hangingwall of low angle shallow detachments illuminated during the 2009 M_w 6.1 L'Aquila seismic sequence. The structural setting of the VFTF can therefore be considered as an analogue of seismically-activated low-angle volumes recently illuminated in the Apennines through seismological methods. Further work to determine the influence of this extension on other thrust faults in the Gran Sasso massif may shed further light on the processes which occur on low-angle faults within extensional regimes.

Acknowledgements

Staff at Rifugio Campo Imperatore, Paolo in particular, are thanked for accommodation and friendly support during field seasons. Microstructural data discussed within this work would not have been carried out effectively but for the patient help of H. Bagshaw and J. Fellows, whose assistance is greatly appreciated. The "Ente Parco Nazionale

del Gran Sasso e Monti della Laga" are also thanked for permission to conduct fieldwork in the Fornaca Valley. Aerial photographs are from the Regione Abruzzo, the use of which is greatly appreciated. Stereonets were produced using Stereonet and Faultkin software by Rick Allmendinger (Marrett and Allmendinger, 1990; Allmendinger et al., 2011; Cardozo and Allmendinger, 2013). This research was funded by the European Research Council Consolidator Grant Project (NOFEAR) No 614705 (principal investigator: Giulio Di Toro). Luca Cardello and Telemaco Tesei are thanked for constructive reviews which improved this manuscript.

References

Adamoli, L., Bigozzi, A., Ciarapica, G., Cirilli, S., Passeri, L., Romano, A., Duranti, F., Venturi, F., 1990. Upper Triassic bituminous facies and Hettangian pelagic facies in the Gran Sasso Range. Bollettino Della Società Geologica Italiana 109, 219–230.

Adamoli, L., Calamita, F., Pizzi, A., 2012. Note illustrative della Carta Geologica d'Italia alla scala 1:50,000, Foglio 349, Gran Sasso d'Italia.

Allmendinger, R.W., Cardozo, N., Fisher, D.M., 2011. Structural Geology Algorithms, Structural Geology Algorithms. Cambridge University Press, Cambridge. https://doi.org/10.1017/CBO9780511920202

Barattolo, F., Bigozzi, A., 1996. Dasycladaleans and depositional environments of the upper Triassic-Liaasic carbonate platform of the Gran Sasso (central Apennines, Italy). Facies 35, 163–208.

Bertinelli, A., Nannarone, C., Passeri, L., Venturi, F., 2004. Hettangian ammonites and radiolarians in the Mt. Camicia (Gran Sasso, Central Apennines). Rivista Italiana Di Paleontologia E Stratigrafia 110, 87–95. https://doi.org/http://dx.doi.org/10.13130/2039-4942/6270

768 Bigi, S., 2006. An example of inversion in a brittle shear zone. Journal of Structural Geology
769 28, 431–443. https://doi.org/10.1016/j.jsg.2005.12.012
770 Billi, A., 2010. Microtectonics of low-P low-T carbonate fault rocks. Journal of Structural
771 Geology 32, 1392–1402. https://doi.org/10.1016/j.jsg.2009.05.007
772 Bos, B., Spiers, C.J., 2001. Experimental investigation into the microstructural and
773 mechanical evolution of phyllosilicate-bearing fault rock under conditions favouring
774 pressure solution. Journal of Structural Geology 23, 1187–1202.
775 https://doi.org/10.1016/S0191-8141(00)00184-X
776 Bullock, R.J., De Paola, N., Holdsworth, R.E., Trabucho-Alexandre, J.J., 2014. Lithological
777 controls on the deformation mechanisms operating within carbonate-hosted faults during
778 the seismic cycle. Journal of Structural Geology 58, 22–42.
779 https://doi.org/10.1016/j.jsg.2013.10.008
780 Caine, J.S., Evans, J.P., Forster, C.B., 1996. Fault zone architechture and permeability
781 structure. Geology 24, 1025–1028. https://doi.org/10.1130/0091-7613(1996)024<1025
782 Cardello, G.L., Doglioni, C., 2015. From Mesozoic rifting to Apennine orogeny: The Gran
783 Sasso range (Italy). Gondwana Research 27, 1307–1334.
784 https://doi.org/10.1016/j.gr.2014.09.009
785 Cardello, G.L., Mancktelow, N.S., 2015. Veining and post-nappe transtensional faulting in
786 the SW Helvetic Alps (Switzerland). Swiss Journal of Geosciences 108, 379–400.
787 https://doi.org/10.1007/s00015-015-0199-7
788 Cardozo, N., Allmendinger, R.W., 2013. Spherical projection with OSXStereonet. Computer
789 & Geosciences 51, 193–205.
790 Centamore, E., Fumanti, F., Nisio, S., 2002. The Central-Northern Apennines geological
791 evolution from Triassic to Neogene time. Bollettino Della Società Geologica Italiana,
792 Volume Speciale 1, 181–197.

793 Chiaraluce, L., Di Stefano, R., Tinti, E., Scognamiglio, L., Michele, M., Casarotti, E.,
794 Cattaneo, M., De Gori, P., Chiarabba, C., Monachesi, G., Lombardi, A., Valoroso, L.,
795 Latorre, D., Marzorati, S., 2017. The 2016 Central Italy Seismic Sequence: A First Look
796 at the Mainshocks, Aftershocks, and Source Models. Seismological Research Letters 88,
797 757–771. https://doi.org/10.1785/0220160221
798 Chiaraluce, L., Valoroso, L., Piccinini, D., Di Stefano, R., De Gori, P., 2011. The anatomy of
799 the 2009 L'Aquila normal fault system (central Italy) imaged by high resolution
800 foreshock and aftershock locations. Journal of Geophysical Research 116, B12311.
801 https://doi.org/10.1029/2011JB008352
802 Ciarapica, G., 2007. Regional and global changes around the Triassic-Jurassic boundary
803 reflected in the late Norian-Hettangian history of the Apennine basins. Palaeogeography,
804 Palaeoclimatology, Palaeoecology 244, 34–51.
805 https://doi.org/10.1016/j.palaeo.2006.06.022
806 Clemenzi, L., Storti, F., Balsamo, F., Molli, G., Ellam, R., Muchez, P., Swennen, R., 2015.
807 Fluid pressure cycles, variations in permeability, and weakening mechanisms along low-
808 angle normal faults: The Tellaro detachment, Italy. Geological Society of America
809 Bulletin 127, 1689–1710. https://doi.org/10.1130/B31203.1
810 D'Agostino, N., Chamot-Rooke, N., Funiciello, R., Jolivet, L., Speranza, F., 1998. The role
811 of pre-existing thrust faults and topography on the styles of extension in the Gran Sasso
812 range (central Italy). Tectonophysics 292, 229–254. https://doi.org/10.1016/S0040-
813 1951(98)00070-5
814 D'Agostino, N., England, P., Hunstad, I., Selvaggi, G., 2014. Gravitational potential energy
815 and active deformation in the Apennines. Earth and Planetary Science Letters 397, 121–
816 132. https://doi.org/10.1016/j.epsl.2014.04.013
817 D'Agostino, N., Mantenuto, S., D'Anastasio, E., Avallone, A., Barchi, M., Collettini, C.,

Radicioni, F., Stoppini, A., Fastellini, G., 2009. Contemporary crustal extension in the Umbria-Marche Apennines from regional CGPS networks and comparison between geodetic and seismic deformation. Tectonophysics 476, 3–12. https://doi.org/10.1016/j.tecto.2008.09.033

Davis, G.H., Bump, A.P., García, P.E., Ahlgren, S.G., 2000. Conjugate Riedel deformation band shear zones. Journal of Structural Geology 22, 169–190. https://doi.org/10.1016/S0191-8141(99)00140-6

Demurtas, M., Fondriest, M., Balsamo, F., Clemenzi, L., Storti, F., Bistacchi, A., Di Toro, G., 2016. Structure of a normal seismogenic fault zone in carbonates: The Vado di Corno Fault, Campo Imperatore, Central Apennines (Italy). Journal of Structural Geology 90, 185–206. https://doi.org/10.1016/j.jsg.2016.08.004

Devoti, R., Riguzzi, F., Cuffaro, M., Doglioni, C., 2008. New GPS constraints on the kinematics of the Apennines subduction. Earth and Planetary Science Letters 273, 163–174. https://doi.org/10.1016/j.epsl.2008.06.031

Dolce, M., Di Bucci, D., 2017. Comparing recent Italian earthquakes. Bulletin of Earthquake Engineering 15, 497–533. https://doi.org/10.1007/s10518-015-9773-7

Falcucci, E., Gori, S., Moro, M., Fubelli, G., Saroli, M., Chiarabba, C., Galadini, F., 2015. Deep reaching versus vertically restricted Quaternary normal faults: Implications on seismic potential assessment in tectonically active regions: Lessons from the middle Aterno valley fault system, central Italy. Tectonophysics 651, 186–198. https://doi.org/10.1016/j.tecto.2015.03.021

Fondriest, M., Aretusini, S., Di Toro, G., Smith, S.A.F., 2015. Fracturing and rock pulverization along an exhumed seismogenic fault zone in dolostones: The Foiana Fault Zone (Southern Alps, Italy). Tectonophysics 654, 56–74. https://doi.org/10.1016/j.tecto.2015.04.015

Fondriest, M., Doan, M.-L., Aben, F., Fusseis, F., Mitchell, T.M., Voorn, M., Secco, M., Di Toro, G., 2017. Static versus dynamic fracturing in shallow carbonate fault zones. Earth and Planetary Science Letters 461, 8–19. https://doi.org/10.1016/j.epsl.2016.12.024

Fondriest, M., Smith, S.A.F., Candela, T., Nielsen, S.B., Mair, K., Di Toro, G., 2013. Mirror-like faults and power dissipation during earthquakes. Geology 41, 1175–1178. https://doi.org/10.1130/G34641.1

Galadini, F., Messina, P., 2004. Early–Middle Pleistocene eastward migration of the Abruzzi Apennine (central Italy) extensional domain. Journal of Geodynamics 37, 57–81. https://doi.org/10.1016/j.jog.2003.10.002

Galli, P., 2002. New paleoseismological data from the Gran Sasso d'Italia area (central Apennines). Geophysical Research Letters 29, 1134. https://doi.org/10.1029/2001GL013292

Ghisetti, F., 1987. Mechanisms of thrust faulting in the gran sasso chain, central apennines, italy. Journal of Structural Geology 9, 955–967. https://doi.org/10.1016/0191-8141(87)90004-6

Ghisetti, F., Vezzani, L., 2002. Normal faulting, transcrustal permeability and seismogenesis in the Apennines (Italy). Tectonophysics 348, 155–168. https://doi.org/10.1016/S0040-1951(01)00254-2

Ghisetti, F., Vezzani, L., 1999. Depth and modes of Pliocene-Pleistocene crustal extension of the Apennines (Italy). Terra Nova 11, 67–72. https://doi.org/10.1046/j.1365-3121.1999.00227.x

Ghisetti, F., Vezzani, L., 1991. Thrust belt development in the central Apennines (Italy): Northward polarity of thrusting and out-of-sequence deformations in the Gran Sasso Chain. Tectonics 10, 904–919. https://doi.org/10.1029/91TC00902

Ghisetti, F.C., Vezzani, L., 1986. Carta Geologica del Gruppo M.Siella-M.Camicia-M.Prena-

M.Brancastello (Gran Sasso d'Italia, Abruzzo) Scale 1:15.000. https://doi.org/10.13140/RG.2.1.5022.1683

Gratier, J.P., Richard, J., Renard, F., Mittempergher, S., Doan, M.L., Di Toro, G., Hadizadeh, J., Boullier, A.M., 2011. Aseismic sliding of active faults by pressure solution creep: Evidence from the San Andreas Fault Observatory at Depth. Geology 39, 1131–1134. https://doi.org/10.1130/G32073.1

Gratier, Dysthe, D.K., Renard, F., 2013a. The Role of Pressure Solution Creep in the Ductility of the Earth's Upper Crust. Advances in Geophysics. 47–179. https://doi.org/10.1016/B978-0-12-380940-7.00002-0

Gratier, Thouvenot, F., Jenatton, L., Tourette, A., Doan, M.L., Renard, F., 2013b. Geological control of the partitioning between seismic and aseismic sliding behaviours in active faults: Evidence from the Western Alps, France. Tectonophysics 600, 226–242. https://doi.org/10.1016/j.tecto.2013.02.013

Hadizadeh, J., 1994. Interaction of cataclasis and pressure solution in a low-temperature carbonate shear zone. Pure and Applied Geophysics PAGEOPH 143, 255–280. https://doi.org/10.1007/BF00874331

Kamb, W.B., 1959. Ice petrofabric observations from Blue Glacier, Washington, in relation to theory and experiment. Journal of Geophysical Research 64, 1891. https://doi.org/10.1029/JZ064i011p01891

Katz, Y., Weinberger, R., Aydin, A., 2004. Geometry and kinematic evolution of Riedel shear structures, Capitol Reef National Park, Utah. Journal of Structural Geology 26, 491–501. https://doi.org/10.1016/j.jsg.2003.08.003

Koopman, A., 1983. Detachment tectonics in the central Apennines, Italy. Instituut voor Aardwetenschappen RUU.

Kuo, L.-W., Song, S.-R., Suppe, J., Yeh, E.-C., 2016. Fault mirrors in seismically active fault

zones: A fossil of small earthquakes at shallow depths. Geophysical Research Letters 43, 1950–1959. https://doi.org/10.1002/2015GL066882

Kuo, L., Li, H., Smith, S.A.F., Di Toro, G., Suppe, J., Song, S.S.-R., Nielsen, S., Sheu, H.-S.H., Si, J., Wenchuan, M., Kuo, L., Li, H., Smith, S.A.F., Toro, G. Di, Suppe, J., Song, S.S.-R., Nielsen, S., Sheu, H.-S.H., Si, J., 2014. Gouge graphitization and dynamic fault weakening during the 2008 Mw 7.9 Wenchuan earthquake. Geology 42, 47–50. https://doi.org/10.1130/G34862.1

Lena, G., Barchi, M.R., Alvarez, W., Felici, F., Minelli, G., 2015. Mesostructural analysis of S-C fabrics in a shallow shear zone of the Umbria–Marche Apennines (Central Italy). Geological Society, London, Special Publications 409, 149–166. https://doi.org/10.1144/SP409.10

Marrett, R., Allmendinger, R.W., 1990. Kinematic analysis of fault-slip data. Journal of Structural Geology 12, 973–986. https://doi.org/10.1016/0191-8141(90)90093-E

Michele, M., Di Stefano, R., Chiaraluce, L., Cattaneo, M., De Gori, P., Monachesi, G., Latorre, D., Marzorati, S., Valoroso, L., Ladina, C., Chiarabba, C., Lauciani, V., Fares, M., 2016. The Amatrice 2016 seismic sequence: A preliminary look at the mainshock and aftershocks distribution. Annals of Geophysics 59. https://doi.org/10.4401/ag-7227

Oohashi, K., Hirose, T., Shimamoto, T., 2011. Shear-induced graphitization of carbonaceous materials during seismic fault motion: Experiments and possible implications for fault mechanics. Journal of Structural Geology 33, 1122–1134. https://doi.org/10.1016/j.jsg.2011.01.007

Ori, G.G., Friend, P.F., 1984. Sedimentary basins formed and carried piggyback on active thrust sheets., Geology. https://doi.org/10.1130/0091-7613(1984)12<475:SBFACP>2.0.CO;2

Pace, P., Calamita, F., 2015. Coalescence of fault-bend and fault-propagation folding in

curved thrust systems: An insight from the Central Apennines, Italy. Terra Nova 27, 175–183. https://doi.org/10.1111/ter.12146

Pace, P., Domenica, A. Di, Calamita, F., 2014. Summit low-angle faults in the Central Apennines of Italy: Younger-on-older thrusts or rotated normal faults? Constraints for defining the tectonic style of thrust belts. Tectonics 33, 756–785. https://doi.org/10.1002/2013TC003385

Ramsay, J.G., 1980. Shear zone geometry: A review. Journal of Structural Geology 2, 83–99. https://doi.org/10.1016/0191-8141(80)90038-3

Rusciadelli, G., Viandante, M.G., Calamita, F., Cook, A.C., 2005. Burial-exhumation history of the central Apennines (Italy), from the foreland to the chain building: thermochronological and geological data. Terra Nova 17, 560–572. https://doi.org/10.1111/j.1365-3121.2005.00649.x

Rutter, E.H., 1983. Pressure solution in nature, theory and experiment. Journal of the Geological Society 140, 725–740. https://doi.org/10.1144/gsjgs.140.5.0725

Rutter, E.H., Hackston, A.J., Yeatman, E., Brodie, K.H., Mecklenburgh, J., May, S.E., 2013. Reduction of friction on geological faults by weak-phase smearing. Journal of Structural Geology 51, 52–60. https://doi.org/10.1016/j.jsg.2013.03.008

Sibson, R.H., 2000. Fluid involvement in normal faulting. Journal of Geodynamics 29, 469–499. https://doi.org/10.1016/S0264-3707(99)00042-3

Siman-Tov, S., Aharonov, E., Boneh, Y., Reches, Z., 2015. Fault mirrors along carbonate faults: Formation and destruction during shear experiments. Earth and Planetary Science Letters 430, 367–376. https://doi.org/10.1016/j.epsl.2015.08.031

Speranza, F., 2003. Genesis and evolution of a curved mountain front: paleomagnetic and geological evidence from the Gran Sasso range (central Apennines, Italy). Tectonophysics 362, 183–197. https://doi.org/10.1016/S0040-1951(02)00637-6

943 Storti, F., Billi, A., Salvini, F., 2003. Particle size distributions in natural carbonate fault
944 rocks: insights for non-self-similar cataclasis. Earth and Planetary Science Letters 206,
945 173–186. https://doi.org/10.1016/S0012-821X(02)01077-4
946 Tarquini, S., Isola, I., Favalli, M., Mazzarini, F., Bisson, M., Pareschi, M.T., Boschi, E.,
947 2007. TINITALY/01: A new Triangular Irregular Network of Italy. Annals of
948 Geophysics 50, 407–425. https://doi.org/10.4401/ag-4424
949 Tarquini, S., Vinci, S., Favalli, M., Doumaz, F., Fornaciai, A., Nannipieri, L., 2012. Release
950 of a 10-m-resolution DEM for the Italian territory: Comparison with global-coverage
951 DEMs and anaglyph-mode exploration via the web. Computers & Geosciences 38, 168–
952 170. https://doi.org/10.1016/j.cageo.2011.04.018
953 Tchalenko, J.S., 1970. Similarities between shear zones of different magnitudes. Bulletin of
954 the Geological Society of America 81, 1625–1640. https://doi.org/10.1130/0016-
955 7606(1970)81[1625:SBSZOD]2.0.CO;2
956 Tesei, T., Collettini, C., Barchi, M.R., Carpenter, B.M., Di Stefano, G., 2014. Heterogeneous
957 strength and fault zone complexity of carbonate-bearing thrusts with possible
958 implications for seismicity. Earth and Planetary Science Letters 408, 307–318.
959 https://doi.org/10.1016/j.epsl.2014.10.021
960 Tesei, T., Collettini, C., Viti, C., Barchi, M.R., 2013. Fault architecture and deformation
961 mechanisms in exhumed analogues of seismogenic carbonate-bearing thrusts. Journal of
962 Structural Geology 55, 167–181. https://doi.org/10.1016/j.jsg.2013.07.007
963 Valoroso, L., Chiaraluce, L., Piccinini, D., Di Stefano, R., Schaff, D., Waldhauser, F., 2013.
964 Radiography of a normal fault system by 64,000 high-precision earthquake locations:
965 The 2009 L'Aquila (central Italy) case study. Journal of Geophysical Research: Solid
966 Earth 118, 1156–1176. https://doi.org/10.1002/jgrb.50130
967 Van Konijnenburg, J.H., Bernoulli, D., Mutti, M., 1999. Stratigraphic architecture of a Lower

968 Cretaceous - Lower Tertiary carbonate base-of-slope succession: Gran Sasso D'Italia
969 (Central Apennines, Italy). SEPM Special Publication 63, 291–315.
970 Vezzani, L., Festa, A., Ghisetti, F.C., 2010. Geology and Tectonic Evolution of the Central-
971 Southern Apennines, Italy. Geological Society of America Special Papers, Geological
972 Society of America Special Papers. Geological Society of America, 1–58.
973 https://doi.org/10.1130/2010.2469
974 Viti, C., Collettini, C., Tesei, T., 2014. Pressure solution seams in carbonatic fault rocks:
975 mineralogy, micro/nanostructures and deformation mechanism. Contributions to
976 Mineralogy and Petrology 167, 970. https://doi.org/10.1007/s00410-014-0970-1
977 Welch, M.J., Davies, R.K., Knipe, R.J., Tueckmantel, C., 2009. A dynamic model for fault
978 nucleation and propagation in a mechanically layered section. Tectonophysics 474, 473–
979 492. https://doi.org/10.1016/j.tecto.2009.04.025
980 Wells, D.L., Coppersmith, K.J., 1994. New Empirical Relationships among Magnitude,
981 Rupture Length, Rupture Width, Rupture Area, and Surface Displacement. Bulletin of
982 the Seismological Society of America 84, 974–1002. https://doi.org/
983 Wojtal, S., Mitra, G., 1986. Strain hardening and strain softening in fault zones from foreland
984 thrusts. Geological Society of America Bulletin 97, 674. https://doi.org/10.1130/0016-
985 7606(1986)97<674:SHASSI>2.0.CO;2
986 Woodcock, N.H., Dickson, J.A.D., Tarasewicz, J.P.T., 2007. Transient permeability and
987 reseal hardening in fault zones: evidence from dilation breccia textures. Geological
988 Society, London, Special Publications 270, 43–53.
989 https://doi.org/10.1144/GSL.SP.2007.270.01.03
990 Yasuhara, H., Marone, C., Elsworth, D., 2005. Fault zone restrengthening and frictional
991 healing: The role of pressure solution. Journal of Geophysical Research 110, B06310.
992 https://doi.org/10.1029/2004JB003327

993

994 **Figure captions**

995

996 **Figure 1:** Maps, cross section, and stratigraphic column of the study area. (a) Map showing
997 the tectonic units and structural setting of the eastern Gran Sasso range; FTW=Fornaca
998 Tectonic Window, MC=Monte Camicia. Modified after Ghisetti and Vezzani (1986). (b)
999 Map of central Italy showing main faults (red=thrust, blue=normal) and location of study area
1000 and map (a) (black rectangle). Adapted from Vezzani et al. (2010). (c) cross section c-c' (see
1001 figure section a) highlighting the structural setting Monte Prena, adjacent to the Fornaca
1002 Tectonic Window. Line of section shown in (a), adapted from Ghisetti and Vezzani (1986).
1003 (d) Stratigraphic column showing lithological units present in thrust sheets adjacent to the
1004 Vado di Ferruccio thrust (VA=Verde Ammonitico, Co=Corniola, Do=Dolomia Principale,
1005 BD=Dolomie Bituminose). Coloured bars indicate the lithologies present within the Miniera
1006 di Lignite (purple) and Santa Colomba (green) thrust sheets. After (Ghisetti, 1987; Adamoli
1007 et al., 1990).

1008

1009 **Figure 2:** Local geometry of the VFTF. Map, modified after Ghisetti and Vezzani (1986),
1010 showing the outcrop of the Fornaca Tectonic Window, and associated cross-sections (A-E)
1011 showing topography and orientation of thrust and normal faulting across the area. Schematic
1012 local sketches illustrate textural variations seen at different localities across the area. For each
1013 section the schematic sketch shows; (A) normal faulting of the thrust core by large later
1014 normal faults, (B) YPR localised shear surfaces in the hangingwall associated with
1015 compressional thrusting, (C) shear folding of S-verging isoclinal folding in the footwall
1016 beneath the fault core and extensional shattering of the hangingwall adjacent to the thrust, (D)
1017 normal faulting cutting mesoscopic S-C fabrics formed in the hangingwall, (E) N-verging

1018 isoclinal folding of marl-rich lithologies. Within local schematic sketches, darker colour
1019 shades illustrate more marl-rich lithologies, red lines represent compressional structures, and
1020 blue lines represent extensional structures. Map grid is in UTM 33T.
1021
1022 **Figure 3:** Structural data summary. Maps and accompanying stereonets showing all of the
1023 763 structural data systematically collected around the Fornaca tectonic window at each
1024 locality. HW=hangingwall, FW=footwall, PSS=principal slip surface, R faults=Riedel faults.
1025 Measurements are presented as poles, average planes and lineations. Red data correspond to
1026 compressional structures, blue data correspond to extensional structures, grey data correspond
1027 to bedding, black dashed lines represent profile planes of folds while black solid data
1028 represent data with no obvious shear sense, green data represent oblique structures.
1029
1030 **Figure 4**: Fault zone exposure and hangingwall damage zone character. Individual photos
1031 show: (a) exposure of the VFTF at the main locality mirror-like surfaces were observed,
1032 black lines mark the upper and lower boundary of the thrust core, (b) nature of damage in the
1033 hangingwall, with traces of hangingwall mirror-like fault surfaces (black) on a face oriented
1034 145/65 (azimuth/dip), (c) sub-centimetre detail of a mirror-surface bordered by
1035 ultracataclasite. All photos were taken at locality 1 (0393004, 4698901).
1036
1037 **Figure 5:** Photograph with accompanying sketch of a meso-scale thrust duplex cut hosting an
1038 S-C fabric cut by a normal fault. The normal fault cuts hangingwall dolomite and the fault
1039 core at locality 2 (0393063, 4698824). Stereonets show: poles to thrust surface (n=8, red
1040 circles), average thrust surface (red great circle), lineation found upon thrust surface (n=1,
1041 hollow red square); poles to normal fault surfaces (n=20, blue circles), average normal fault
1042 surface (blue great circle), lineations upon normal fault surfaces (n=18, hollow blue squares);

poles to S surfaces (n=29, black circles), average S surface fault (black great circle), lineations on S surfaces (n=13, hollow black squares); poles to C surfaces (n=19, black circles), average C surface (black great circle). Arrow on inset map shows location photograph was taken (see Figure 2).

Figure 6: Morphology of slip surfaces. Photos show the principal slip surface in bitumen-poor (a) and bitumen-rich dolomite (b) and mirror surfaces in the hanging wall in bitumen-poor (c) and bitumen-rich dolomite (d). Hanging wall (HW), fault core (FC), and principal slip surface (PSS) are labelled on photographs. Black arrow in (a) is parallel to the on-plane lineation, a lineation is not present in (b). Pencil is parallel to lineation on HW mirror surface in (c). Photos were taken at localities 1 (a & c; 0393004, 4698901), 4 (b; 0393214, 4698893), and 5 (d; 0392815, 4698855).

Figure 7: Character of folding of the interbedded marl-grainstone Corniola in the footwall. Marl rich lithologies in the east (a) form isoclinal folds with S-dipping grainstone bed limbs within a marl-rich matrix. Beneath the fault core (b) isoclinally-folded grainstone beds are cut by thrust parallel reverse faults with minor folding adjacent to fault surfaces. Adjacent to the fault core (c) isoclinal folds in grainstone-rich beds are refolded around an axial plane oriented subparallel to the main thrust. Photos were taken at localities 1 (b & c; 0393004, 4698901), and 4 (a; 0393214, 4698893).

Figure 8: Variation of fault core lithologies across the area. Red stars show locations samples were collected for microanalysis. Stacked bar graphs show percentage area coverage of thrust core lithologies derived from the sketches above without accounting for clast/grain size.

Thrust shear sense is indicated by red arrows. Locations of localities can be seen in Figures 2 & 3.

Figure 9: Microstructural summary of clay-enriched fault core rocks. Sample location is shown as a red star upon a field photo of S-C tectonites in (a). Sense of shear in (a) is consistent throughout all images. High resolution scan (b) and associated sketch (c) show the location of stitched plane-polarised light optical photomicrograph (d) as red rectangle. Points (e,f,g) in (d) indicate locations of point raman spectroscopic analyses, the spectra for which are indicated below, labelled with the dominant species visible from raman shift peaks; amorphous carbon (e), dolomite (f), and calcite (g). SEM-BSE images (h & i) show interactions of calcite (cc) veining through a dolomite matrix (dol) hosting pressure solution seams (PS). Microshears in (h) almost always cut NE-dipping veins rather than SW dipping veins. SW-dipping veins in (i) are truncated by an R-shear, offsetting PS-rich areas of the matrix. This shear surface has been reactivated as a PS seam due to stress inversion. Sub-vertical arrows labelled σ_{e1} in parts (h) & (i) indicate orientation of effective maximum compressive stress within the fault core, assuming parallel vein orientation and perpendicular pressure solution seam formation. Sample was collected at Locality 1 (0393004, 4698901).

Figure 10: Microstructural summary of clay-poor fault core lithologies. Stitched cross-polarised optical photomicrographs (a) show multiple mutually-offsetting filled hybrid fracture vein sets (V1-V3). Inset photographs show location of sample within fault core (red star) and field view of dark-coloured veins in (a). Optical photomicrograph (b) of the matrix of separate clay-poor fault core rocks shows recrystallised fossils (arrow labelled f), lobate grain boundaries (arrow labelled g), and curved twinning within calcite crystals (arrow labelled t). SEM-BSE images show isolated pressure solution (PS) seams within the

1092 homogenous calcite matrix (c), within which calcite veins occur (d). Samples were collected
1093 at Locality 1 (0393004, 4698901).
1094
1095 **Figure 11:** Kinematics of mirror-like hangingwall normal faults and schematics of structures
1096 found in the thrust zone. Stereonets show the distribution of (a) mirror-like fault surfaces, (b)
1097 slip lineations on mirror-like fault surfaces (contoured after Kamb (1959), intervals of 2 and
1098 significance level of 3), (c) hanging wall transport directions, (d) mirror-surface fault
1099 lineations at locality one (blue) and fault core principal slip surface lineations at locality one
1100 (red), (e) focal mechanism derived from kinematic inversion of 133 mirror-like faults in the
1101 hangingwall damage zone of the VFTF (sensu Marrett and Allmendinger, 1990). All
1102 Stereonets are lower hemisphere equal area projections. Schematic sketches show mesoscale
1103 structures in the thrust zone (f) with reference to figure where feature is shown, and
1104 microscale features in clay-enriched (g) and clay-poor (h) fault rocks. In mesoscale sketch (f),
1105 kinematic mechanism is Fig. 11e viewed parallel to thrust strike. Micro-scale sketches show
1106 microstructural features rotated based on average thrust core dip, compressional structures are
1107 coloured red and extensional features coloured blue. Red and blue arrows show the effective
1108 principal compressive stress orientation derived from microstructures for compressional and
1109 extensional stress regimes, respectively. Pressure solution is labelled PS and successive vein
1110 sets labelled V1-V3 (V3 is the most recent).
1111
1112 **Figure 12:** Comparison of kinematics and geometry of hanging wall volumes activated on
1113 the VFTF and in the L'Aquila 2009 M_w 6.1 seismic sequence. **VFTF**: (a) cross section
1114 indicating the location of the measured kinematics used to construct focal mechanisms
1115 (locality 1; see Fig. 2 for further detail of location). Focal mechanisms are derived from (b)
1116 133 mirror-surfaced faults in the hangingwall of the VFTF, and (c) 2 lineations and 30 fault

plane measurements collected on the principal slip surface on the boundary between the thrust core and hangingwall on the VFTF. **L'Aquila**: Cross sections (after Valoroso et al., 2013) indicating the distribution and typical focal mechanisms of fore and aftershocks during the 2009 M_w 6.1 L'Aquila seismic sequence.

Table caption

Table 1: Table of dominant microstructures, inferred deformation processes, and kinematics.

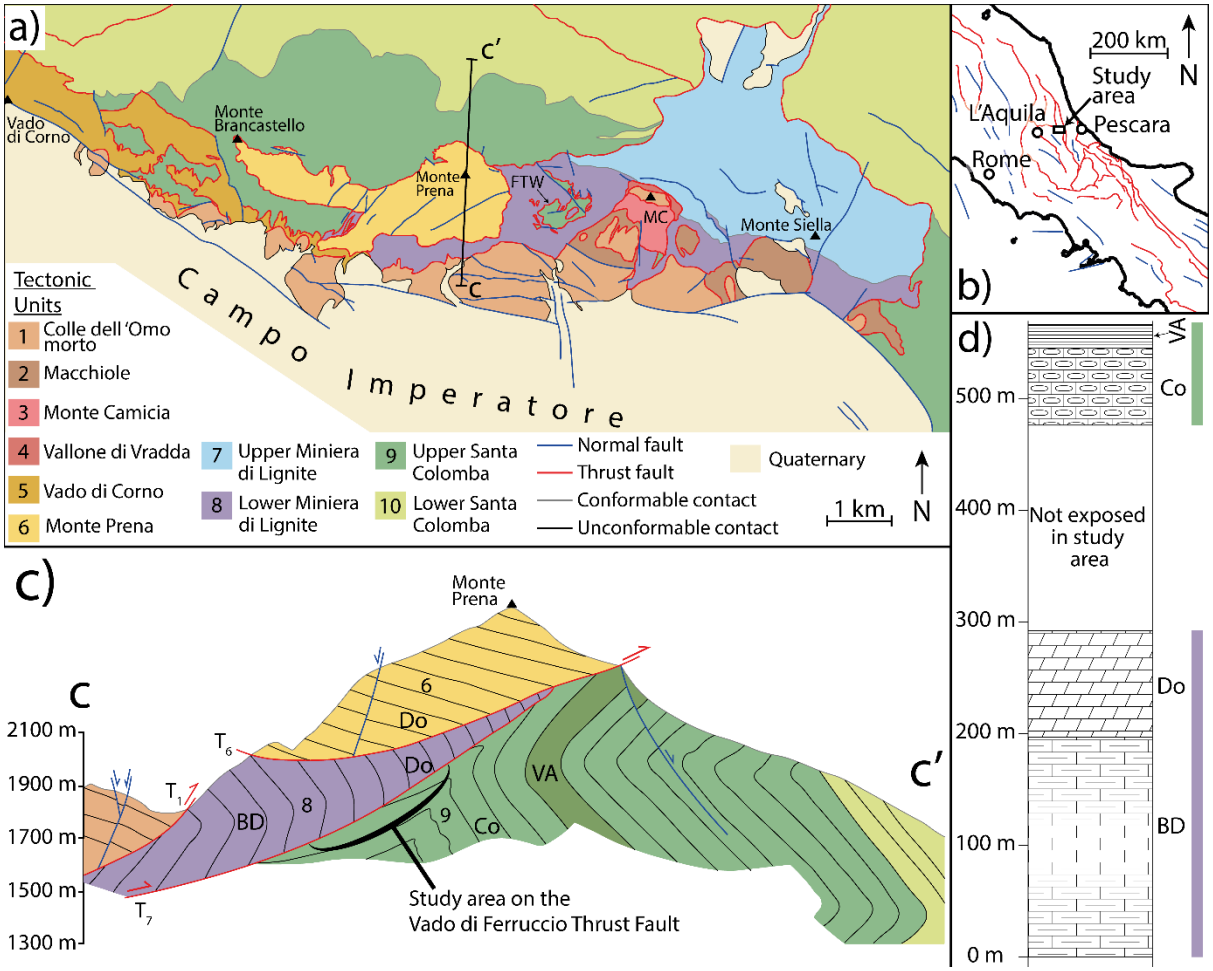
a)
c'
c
Vado
di Corno
Monte
Brancastello
Monte
Prena
FTW
MC
Monte Siella
Campo Imperatore
Tectonic
Units
1 Colle dell 'Omo morto
2 Macchiole
3 Monte Camicia
4 Vallone di Vradda
5 Vado di Corno
6 Monte Prena
7 Upper Miniera di Lignite
8 Lower Miniera di Lignite
9 Upper Santa Colomba
10 Lower Santa Colomba
Normal fault
Thrust fault
Conformable contact
Unconformable contact
Quaternary
1 km
N
b)
200 km
N
Study
area
L'Aquila
Pescara
Rome
c)
Monte
Prena
c
c'
2100 m
1900 m
1700 m
1500 m
1300 m
T6
T1
T7
6
Do
Do
VA
BD
8
9
Co
Study area on the
Vado di Ferruccio Thrust Fault
d)
500 m
400 m
300 m
200 m
100 m
0 m
VA
Co
Not exposed
in study
area
Do
BD

Figure 1

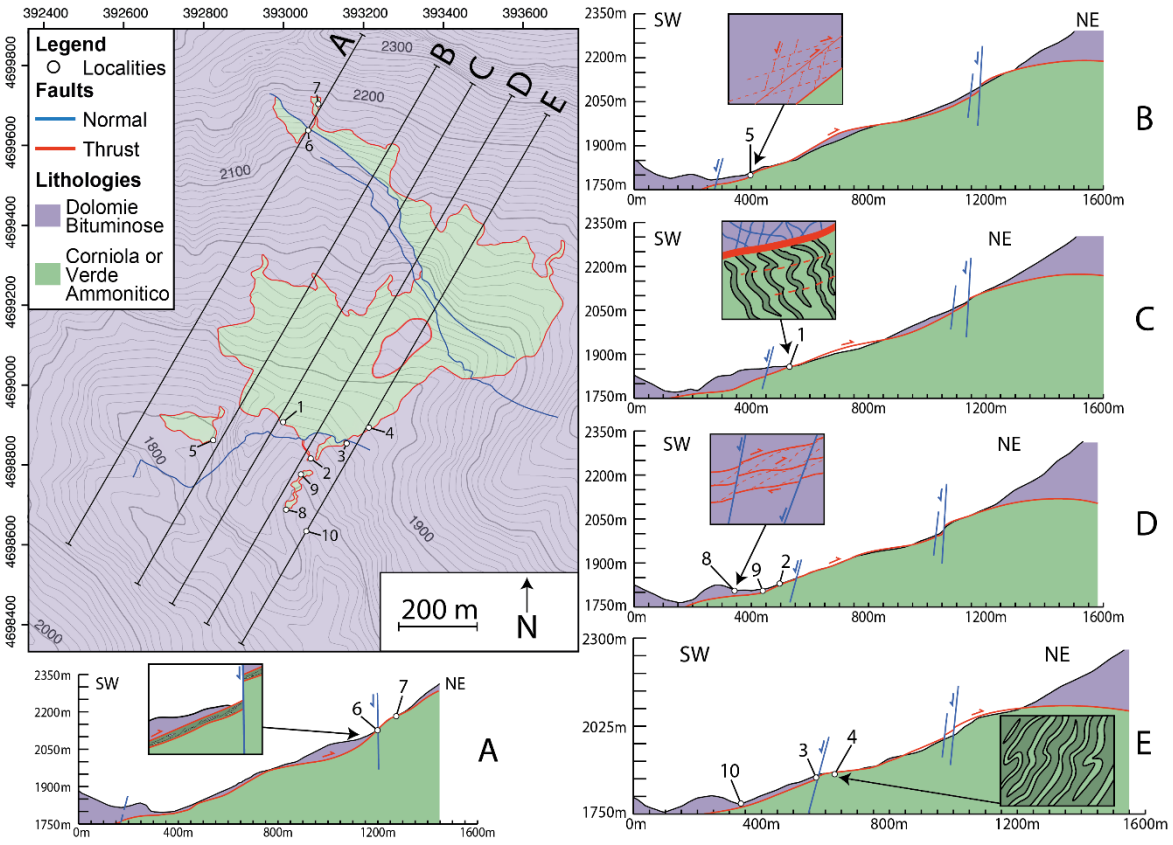

1129

1130 **Figure 2**

1131

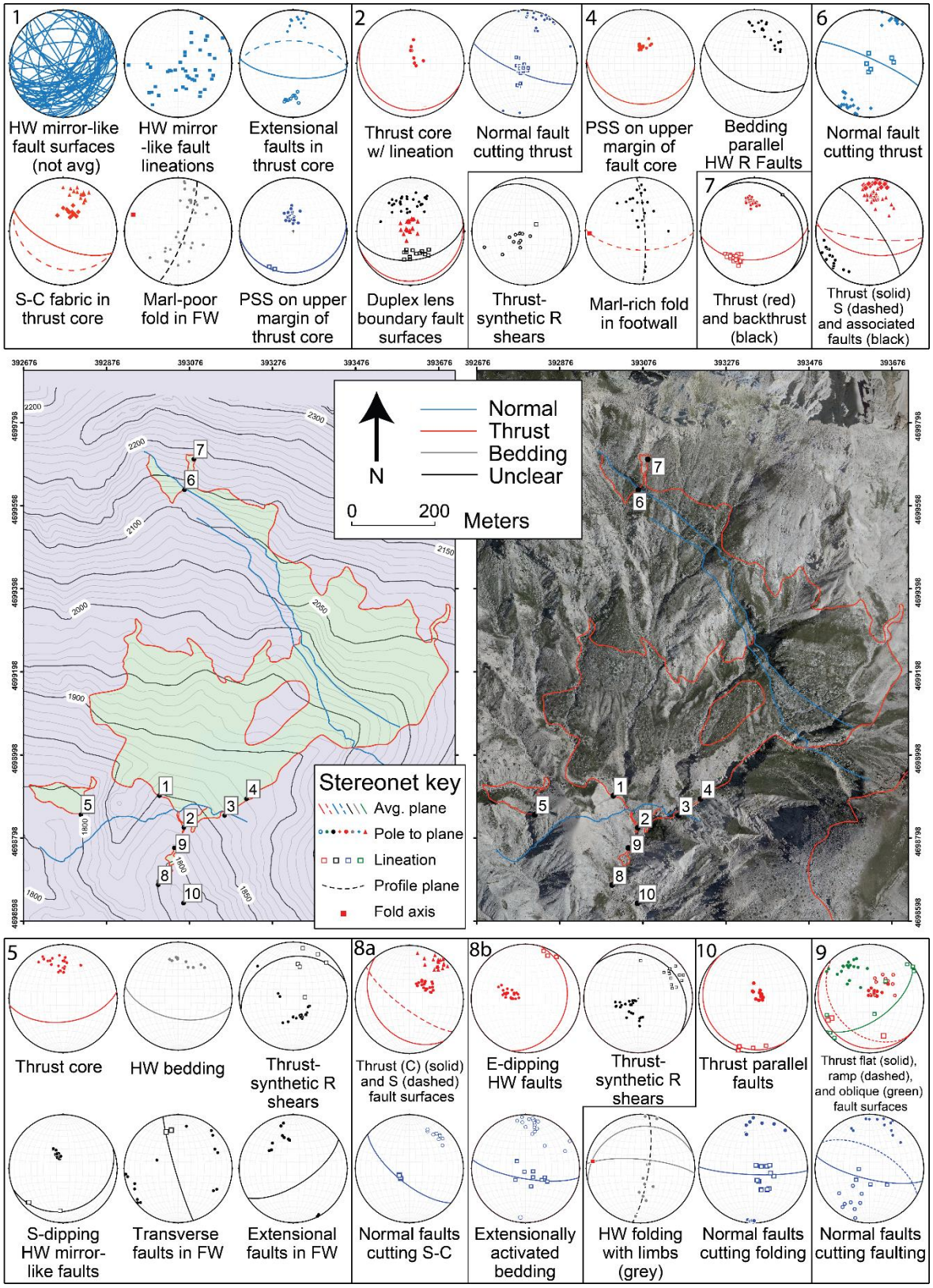
1
HW mirror-like fault surfaces (not avg)
HW mirror -like fault lineations
Extensional faults in thrust core
S-C fabric in thrust core
Marl-poor fold in FW
PSS on upper margin of thrust core
2
Thrust core w/ lineation
Normal fault cutting thrust
Duplex lens boundary fault surfaces
Thrust-synthetic R shears
4
PSS on upper margin of fault core
Bedding parallel HW R Faults
Marl-rich fold in footwall
7
Thrust (red) and backthrust (black)
6
Normal fault cutting thrust
Thrust (solid) S (dashed) and associated faults (black)
N
Normal
Thrust
Bedding
Unclear
0
200
Meters
Stereonet key
Avg. plane
Pole to plane
Lineation
Profile plane
Fold axis
5
Thrust core
HW bedding
Thrust-synthetic R shears
S-dipping HW mirror-like faults
Transverse faults in FW
Extensional faults in FW
8a
Thrust (C) (solid) and S (dashed) fault surfaces
Normal faults cutting S-C
8b
E-dipping HW faults
Thrust-synthetic R shears
Extensionally activated bedding
HW folding with limbs (grey)
10
Thrust parallel faults
Normal faults cutting folding
9
Thrust flat (solid), ramp (dashed), and oblique (green) fault surfaces
Normal faults cutting faulting

Figure 3

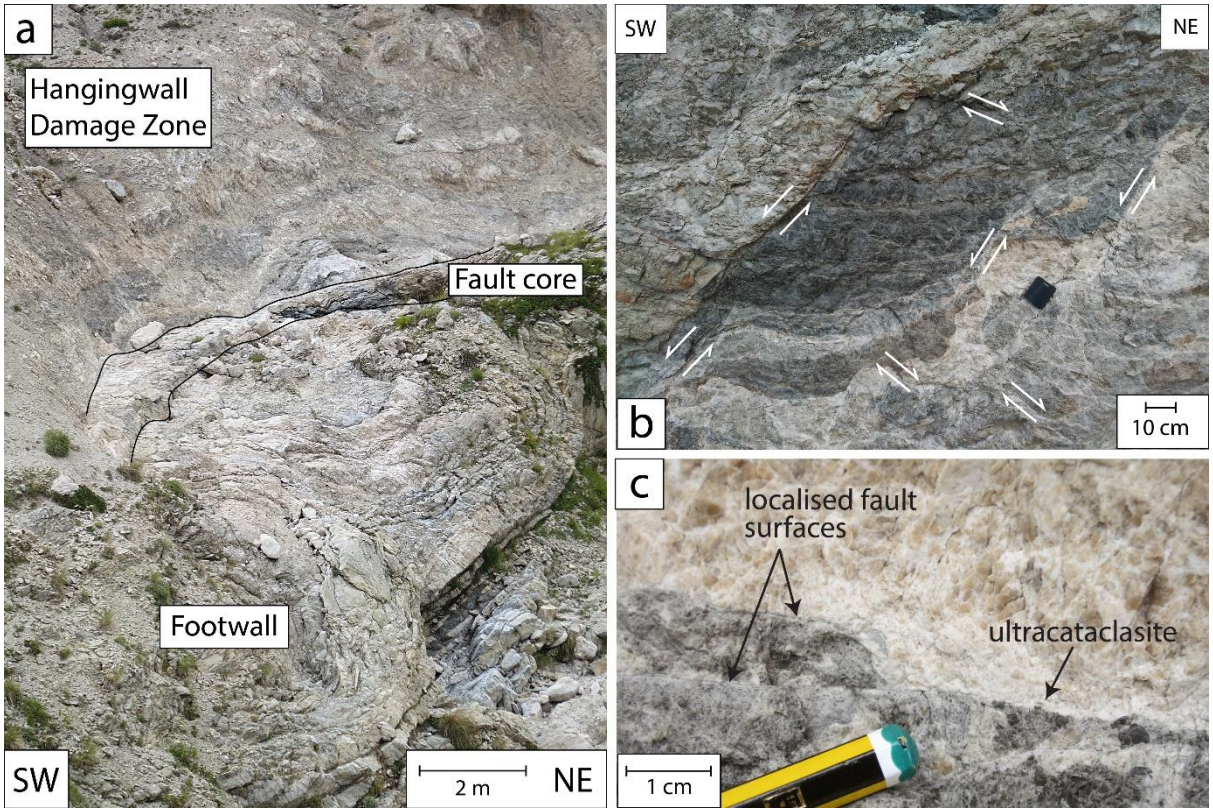
a
Hangingwall
Damage Zone
Fault core
Footwall
SW
2 m
NE
SW
NE
b
10 cm
c
localised fault
surfaces
ultracataclasite
1 cm

Figure 4

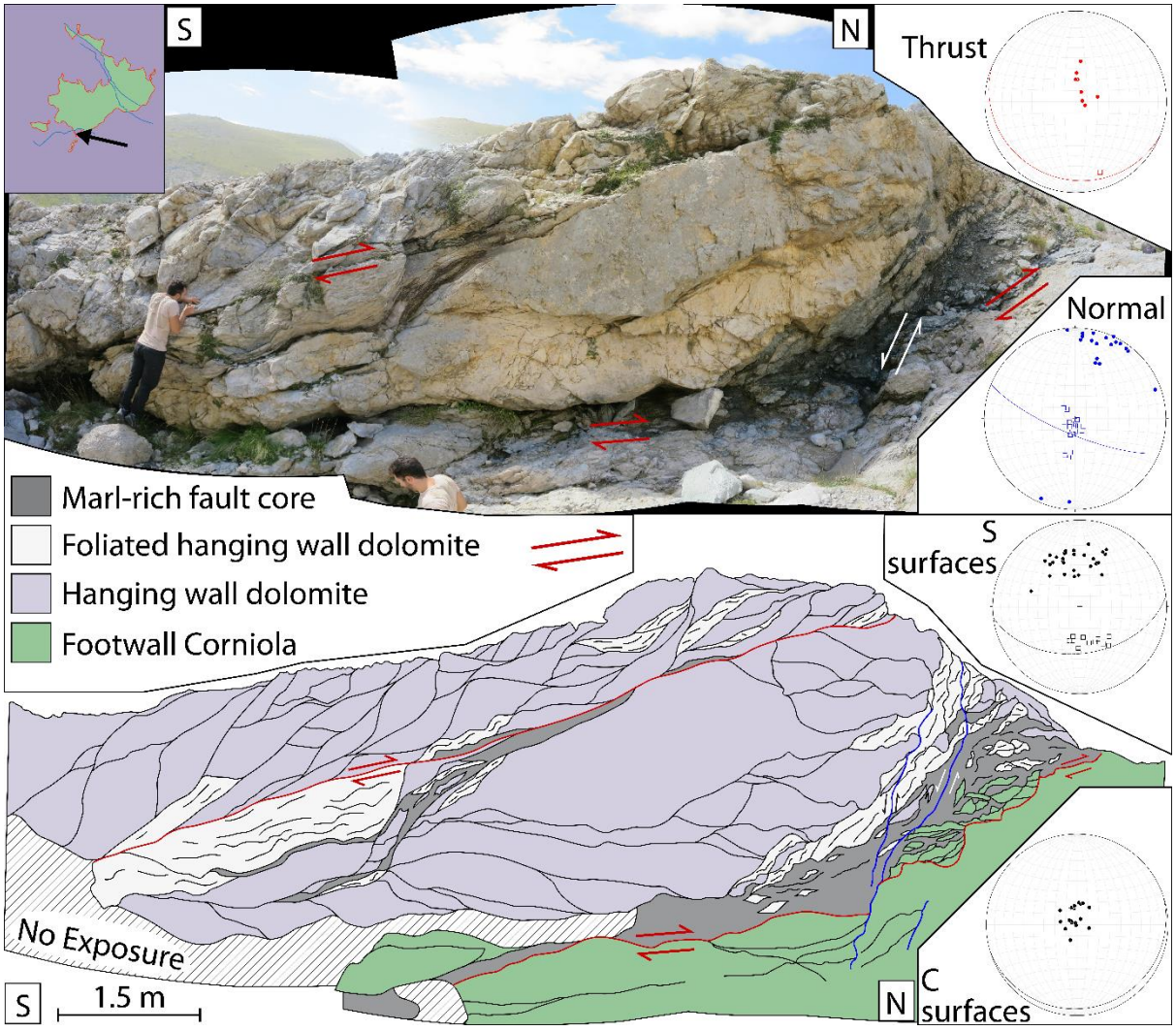

1138

1139 **Figure 5**

1140

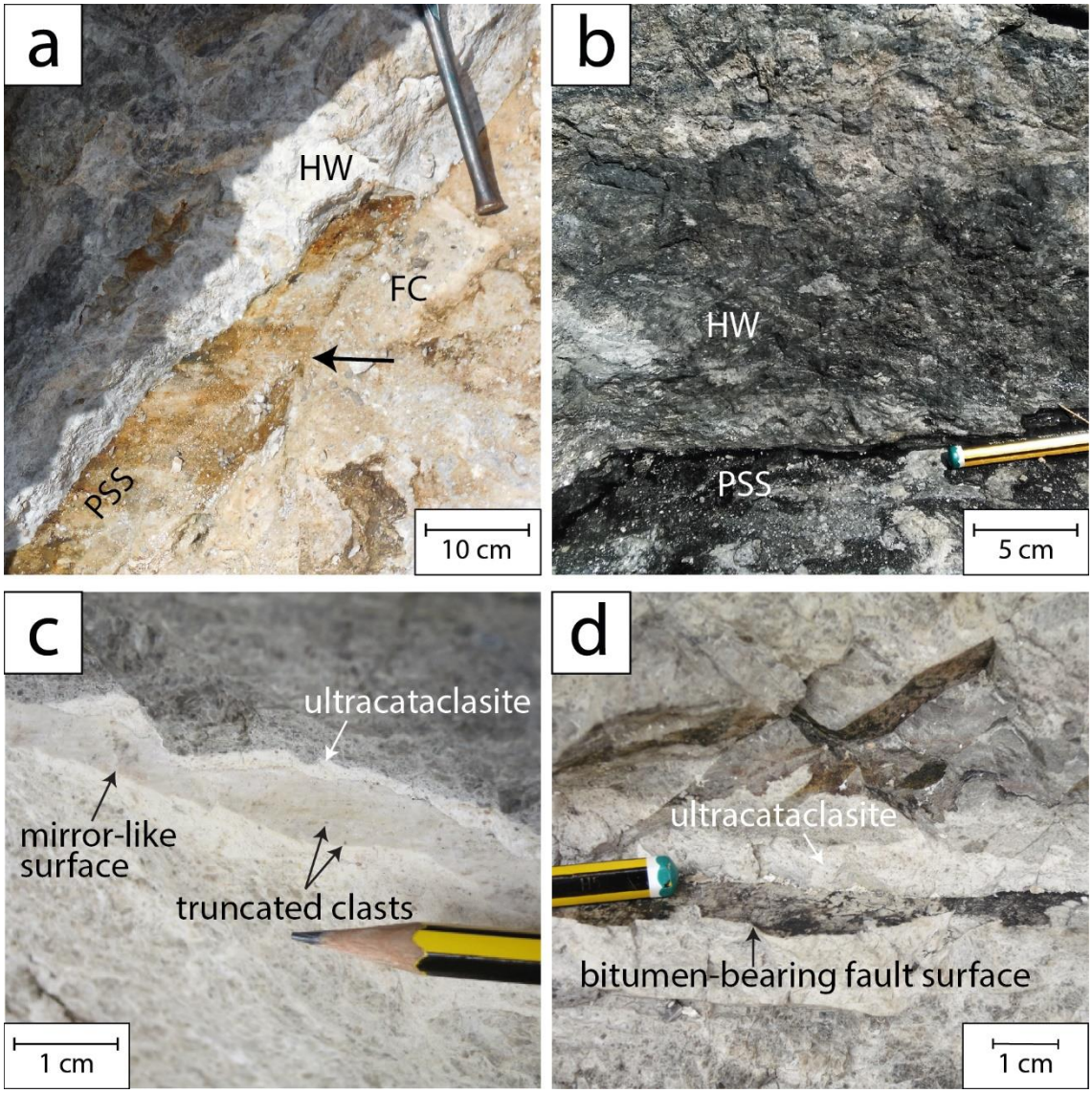

1141

1142 **Figure 6**

1143

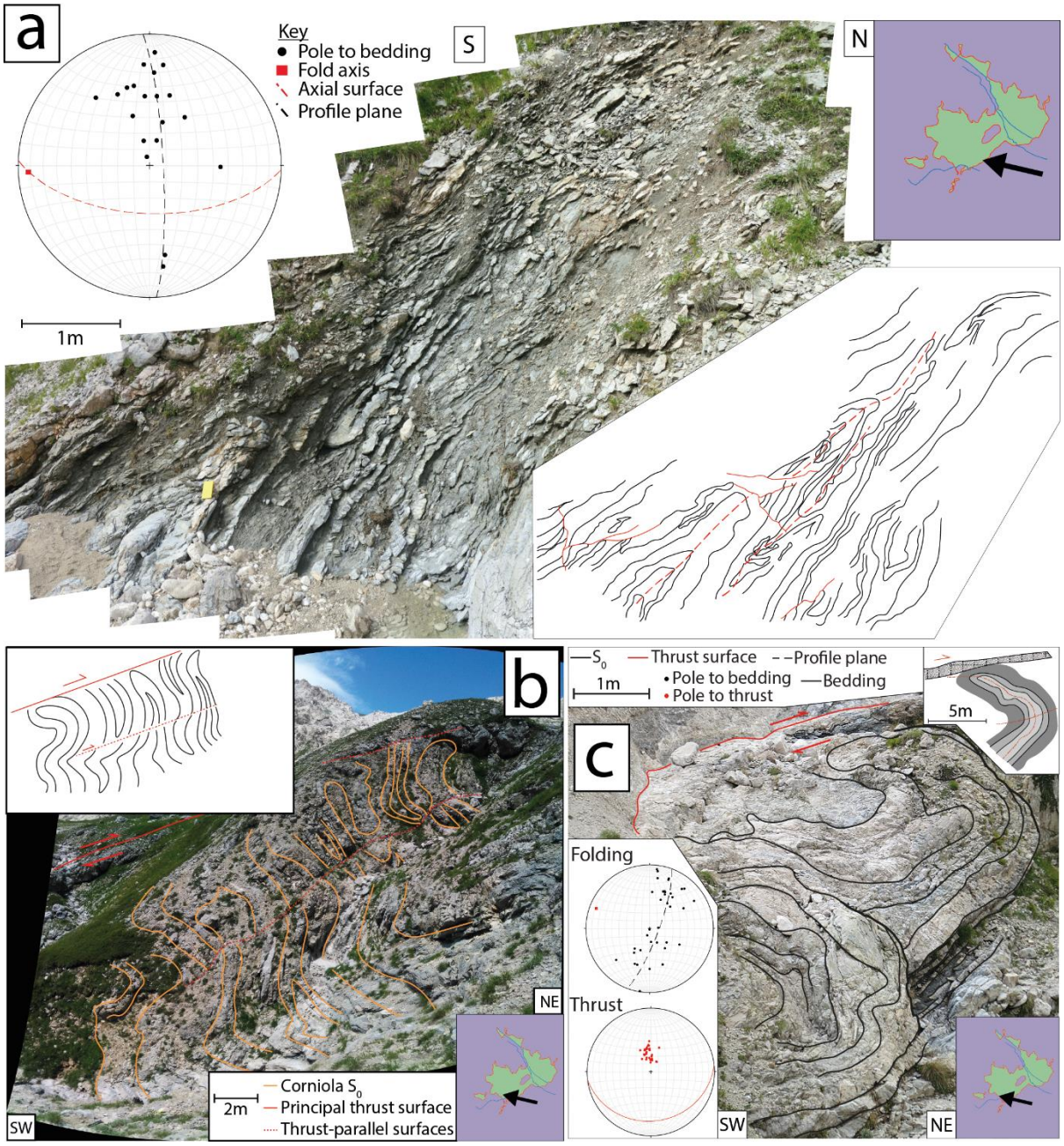

1144

1145 **Figure 7**

1146

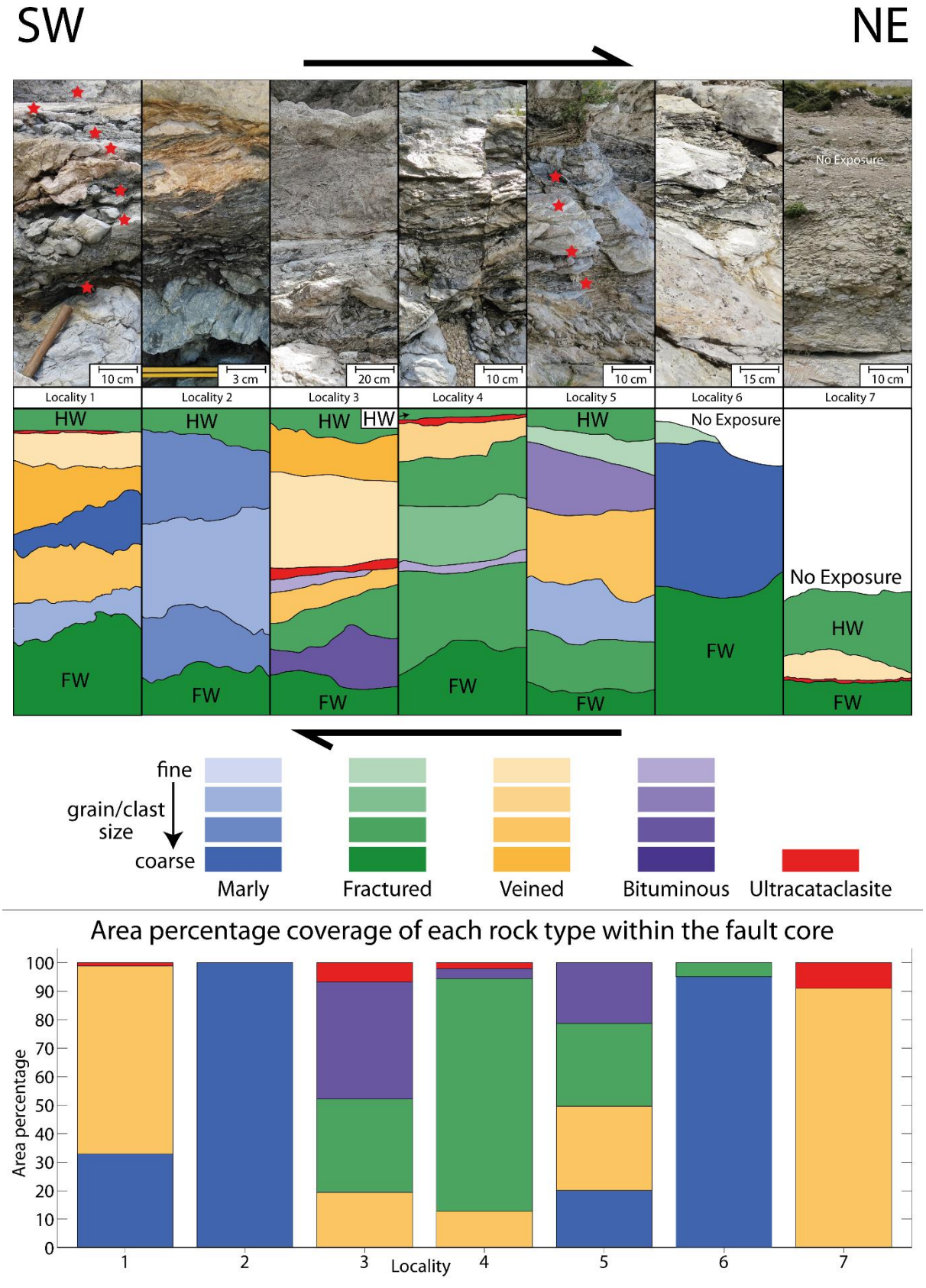
SW
NE
No Exposure
10 cm
3 cm
20 cm
10 cm
10 cm
15 cm
10 cm
Locality 1
Locality 2
Locality 3
Locality 4
Locality 5
Locality 6
Locality 7
HW
FW
No Exposure
fine
grain/clast size
coarse
Marly
Fractured
Veined
Bituminous
Ultracataclasite
Area percentage coverage of each rock type within the fault core
Area percentage
Locality
0
10
20
30
40
50
60
70
80
90
100
1
2
3
4
5
6
7

Figure 8

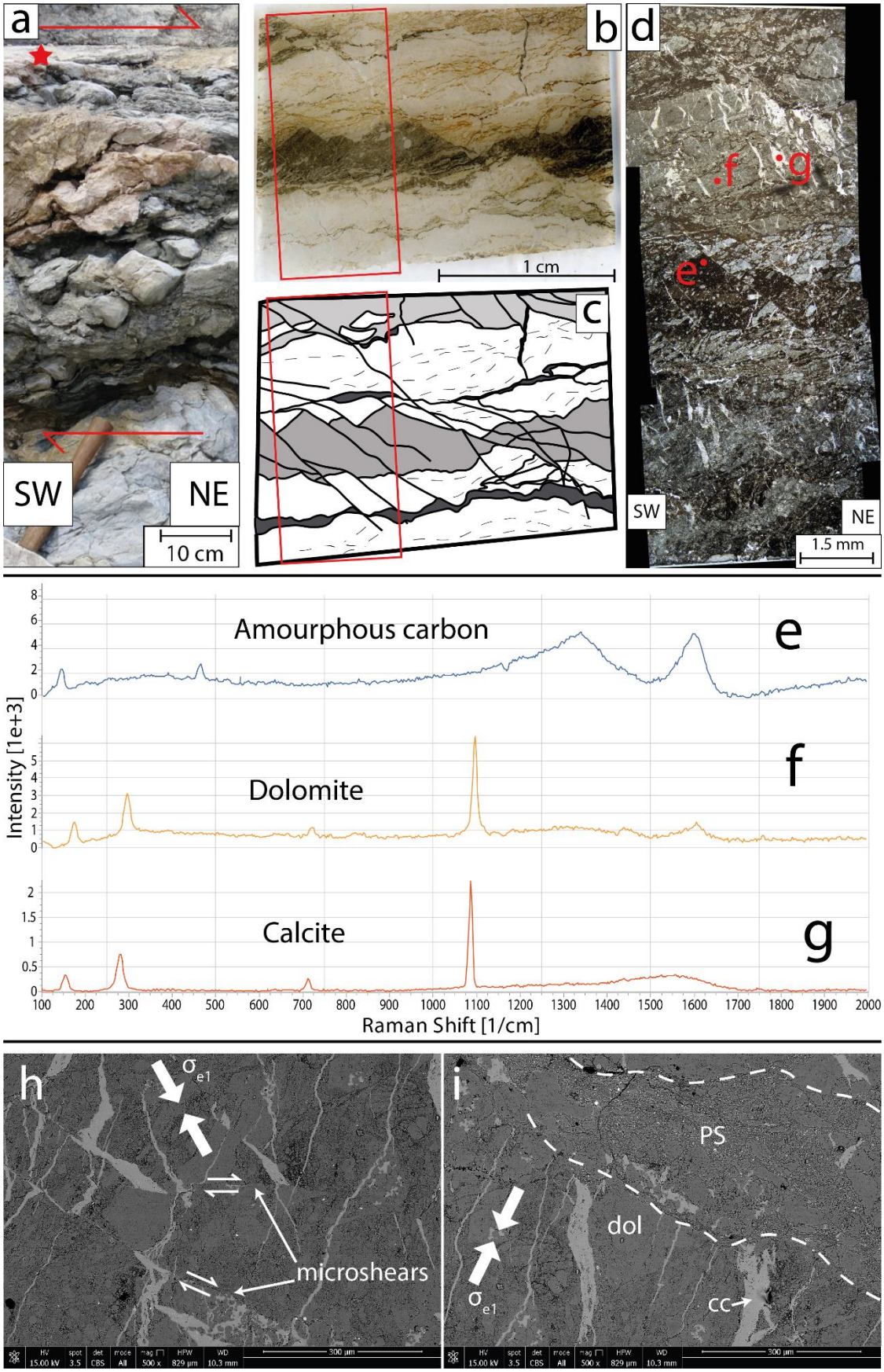
a
b
c
d
SW
NE
10 cm
1 cm
.f
.g
e
SW
NE
1.5 mm
Amourphous carbon
e
Dolomite
f
Calcite
g
Intensity [1e+3]
Raman Shift [1/cm]
h
σ_{e1}
microshears
i
PS
dol
cc
σ_{e1}

Figure 9

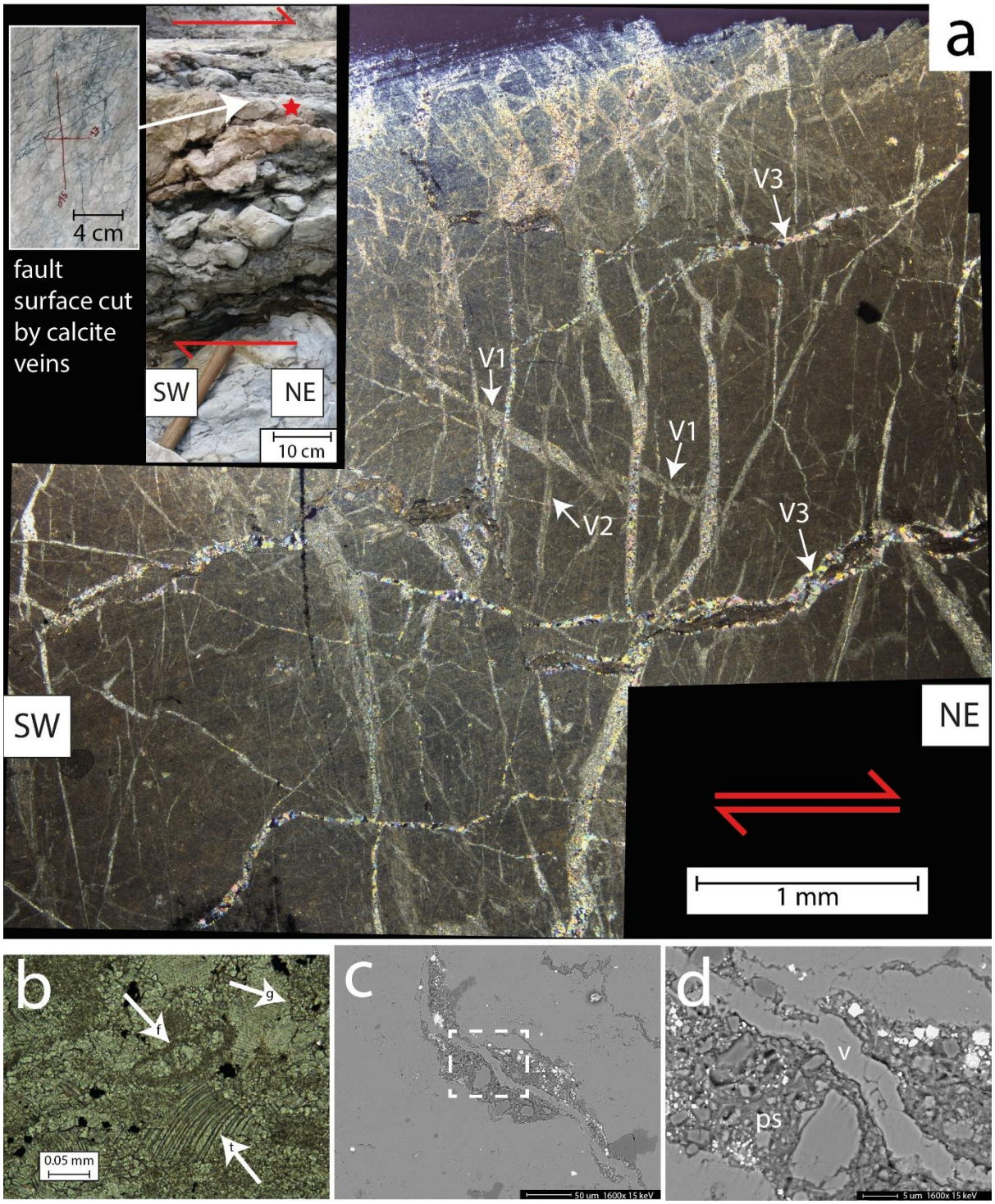
a
4 cm
fault
surface cut
by calcite
veins
SW
NE
10 cm
V1
V2
V3
V1
V3
SW
NE
1 mm
b
f
g
t
0.05 mm
c
d
v
ps

Figure 10

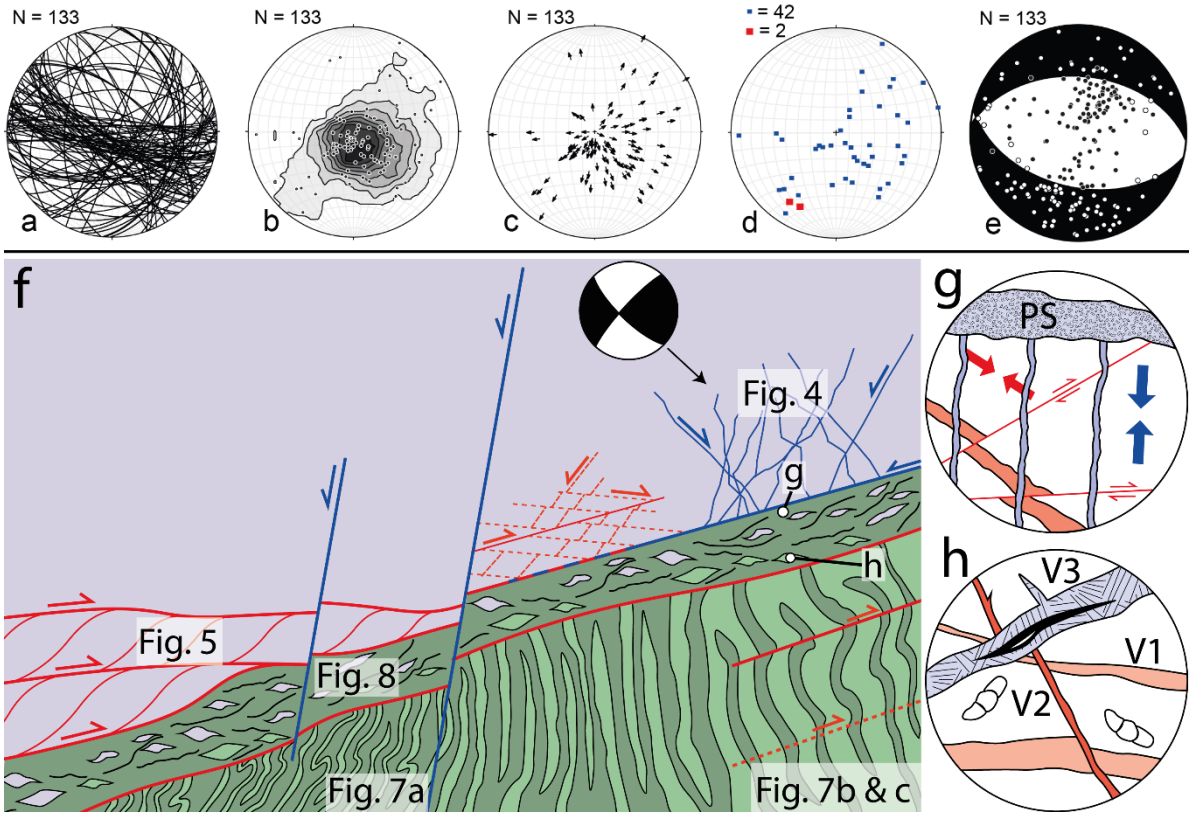
N = 133
N = 133
N = 133
= 42
= 2
N = 133
a
b
c
d
e
f
Fig. 4
g
h
Fig. 5
Fig. 8
Fig. 7a
Fig. 7b & c
g
PS
h
V3
V1
V2

Figure 11

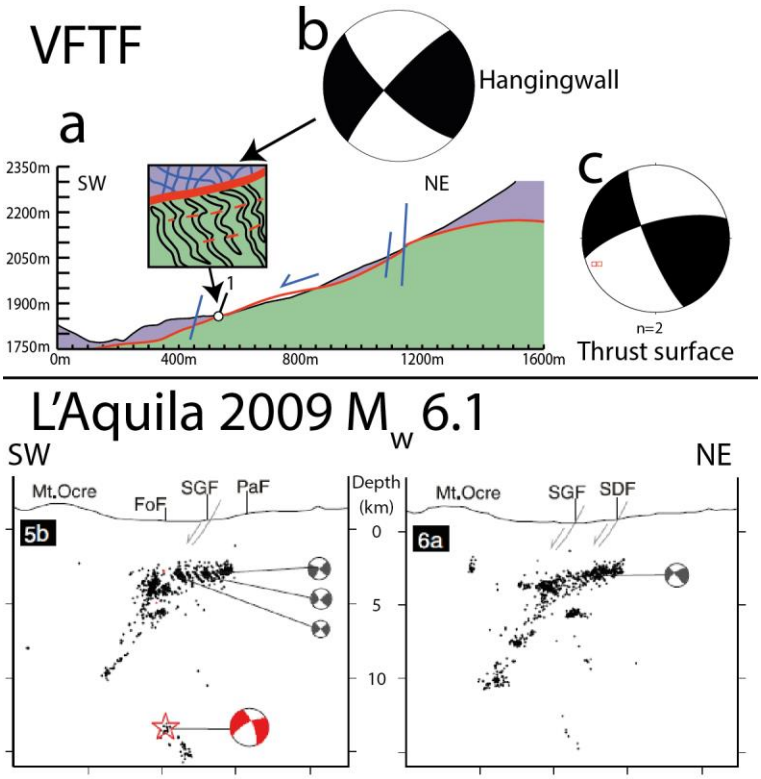
VFTF
a
b
Hangingwall
c
SW
NE
2350m
2200m
2050m
1900m
1750m
0m
400m
800m
1200m
1600m
1
n=2
Thrust surface
L'Aquila 2009 M w 6.1
SW
NE
Mt.Ocre
FoF
SGF
PaF
5b
Depth
(km)
0
5
10
Mt.Ocre
SGF
SDF
6a

Figure 12

Fault rock type	Dominant microstructures	Inferred deformation processes	Inferred kinematics
Clay-enriched (Figure 9)	Lenses of angular fractured grains of variable size	Initial cataclastic grain size reduction	Compressional thrusting
	Clay-rich pressure solution seams containing oxides	Diffusion-controlled pressure solution-mediated stable sliding aided by the presence of clays and fluids	Compressional thrusting
	Calcite veins with varying orientation and opening directions	Veining episodes due to cyclic fluid overpressure	Compressional thrusting and extensional stress regime
	Smaller sharp microfault surfaces cutting veins of certain orientation	Failure between veining episodes due to cyclic fluid overpressure	Compressional thrusting
	Larger north-dipping microfaults with clays and oxides upon fault surface offsetting clay-rich and cataclastic regions and cutting veins	Major rock failure prior to pressure solution upon fine-grained fault surfaces then reactivation of microfault surfaces as pressure solution seams by extensional stress	Failure during compressional thrusting, pressure solution during extensional stress regime
	Well-developed sub-horizontal pressure solution seams, cutting texture and intruding into most recent vein generations	Recent pressure solution, locally developed horizontal response to sub-vertical principal stresses	Extensional stress regime
Clay-poor (Figure 10)	Multiple sets of cross-cutting veins offsetting each other (Fig. 10a)	Veining episodes due to fluid overpressure in variable strain environments forming veins of different orientations	Compressional thrusting and extensional reactivation
	Isolated pressure solution seams, often concurrent with quartz or dolomite grains within calcitic matrix (Fig. 10a,c)	Diffusion-controlled pressure solution, aided by diffusion upon polymineralic grain boundaries	Compressional thrusting and extensional stress regime
	Curved complex calcite twinning of variable degrees of intensity (Fig. 10b)	Irregular twinning due to texture-dependent stress within the fault core	Compressional thrusting and extensional stress regime
	Angular fractured grains of varied size cut by microfaults	Cataclastic grain size reduction and flow	Compressional thrusting
Hanging wall	Heavily fractured angular grains	Cataclasis in the hanging wall adjacent to the thrust surface	Compressional thrusting and hangingwall activation
	Clay-bearing microfault surfaces	Failure and possible minor pressure solution localised in dolomite over a prolonged period	Compressional thrusting and hangingwall activation
	Mirror fault surfaces (Fig. 6)	Velocity-weakening slip and thermal decomposition at high slip rate	Hangingwall activation

Table 1